# Precision Measurement of Lead Isotope Shifts using Two-Laser Excitation and Co- and Counter-Propagating Beams Method

by
Gautam Ramasamy

Professor Protik K. Majumder, Advisor

A thesis submitted in partial fulfillment
of the requirements for the
Degree of Bachelor of Arts with Honors
in Physics

WILLIAMS COLLEGE
Williamstown, Massachusetts
May 25, 2026

# Abstract

We present a new method for measuring transition isotope shifts in lead using a two-step Doppler-free excitation scheme. A fiber electro-optic modulator adds tunable sidebands to the 939 nm first-step laser, and the co- and counter-propagating peak separations are recorded as a function of modulation frequency. Their intersection yields both the 939 nm and 406 nm transition isotope shifts directly, with the result tied to an RF frequency reference and immune to first-step laser drift. We identify a $\sim$2% systematic in the fitted slopes due to Doppler weighting of the Lorentzian lineshapes, and show that it cancels at the intersection point. Applying this co-counter crossing method to $^{204}$Pb/$^{208}$Pb, we obtain $IS_{939}^{204/8} = 381.2 \pm 0.7$ MHz and $IS_{406}^{204/8} = -4589.7 \pm 1.6$ MHz, a $\sim$20% reduction in uncertainty in the first step transition over the naive single-carrier method with the same amount of data.

# Executive Summary

Precision isotope shift measurements in heavy atoms like lead provide critical benchmarks for relativistic many-body atomic structure calculations. With four valence electrons and strong relativistic effects near the nucleus, Pb sits in the regime where state-of-the-art methods—such as configuration interaction plus all-order (CI+all-order) [1]—are most challenged.

We use a two-step Doppler-free excitation scheme [2] to probe Pb isotope shifts. A 939 nm laser drives the first-step transition ($6p^2\ {}^3P_0 \rightarrow 6p^2\ {}^3P_2$), selecting a narrow velocity class from the thermal distribution of atoms in a quartz vapor cell at $\sim$815 °C. A scanning 406 nm external-cavity diode laser drives the second step, detected via lock-in detection. Co- and counter-propagating beam alignments produce isotope peaks at different Doppler-shifted frequencies, and the peak separations in each alignment encodes both transition isotope shifts (Fig. 1).

The simplest approach—measuring peak separations from a single scan pair—provides no consistency checks and is susceptible to systematic bias from Doppler-weighting of the Lorentzian lineshapes. This thesis proposes and demonstrates a new technique, the *co-counter crossing method*, which eliminates this bias. A fiber-coupled electro-optic modulator adds tunable sidebands at $\pm\omega_{\mathrm{mod}}$ to the 939 nm beam. The co- and counter-aligned peak separations $PS_{co}$ and $PS_{ctr}$ are linear in $\omega_{\mathrm{mod}}$ with slopes $\mp 2\,k_{406}/k_{939}$, intersecting at $(\omega_{\mathrm{mod}},\, PS)_{\mathrm{int}} = (IS_{939}^{204/8}/2,\ -IS_{406}^{204/8})$, so both isotope shifts are read directly from the crossing point (Fig. 2). The laser offset cancels exactly, making the result insensitive to lock-point drifts. The crossing point also eliminates the Doppler-weighting bias: simulations confirm that while this systematic may change the slopes by $\sim$2%, the intersection is unaffected. Additionally, the $x$-coordinate of the crossing is tied to an RF synthesizer, providing an *in-situ* frequency reference independent of the Fabry–Pérot cavity.

As a proof of concept, we measure the $^{204}$Pb/$^{208}$Pb transition isotope shifts at seven modulation frequencies spanning 170–230 MHz. Each scan is frequency-calibrated using a Fabry–Pérot Airy-function fit, and a 14-Lorentzian model (one carrier and six sidebands per isotope) extracts peak separations (Fig. 4). Linear fits with Monte Carlo–verified uncertainty propagation yield

$$IS_{939}^{204/8} = 381.2 \pm 0.7 \text{ MHz},$$
$$IS_{406}^{204/8} = -4589.7 \pm 1.6 \text{ MHz},$$

a $\sim$20% reduction in uncertainty over the naive method. With the method validated, the next steps are to calibrate the Fabry–Pérot free spectral range, measure all remaining isotope

pairs—including $^{207}$Pb, whose hyperfine structure can be resolved using the same sideband technique—and extend to a second set of Pb transitions.

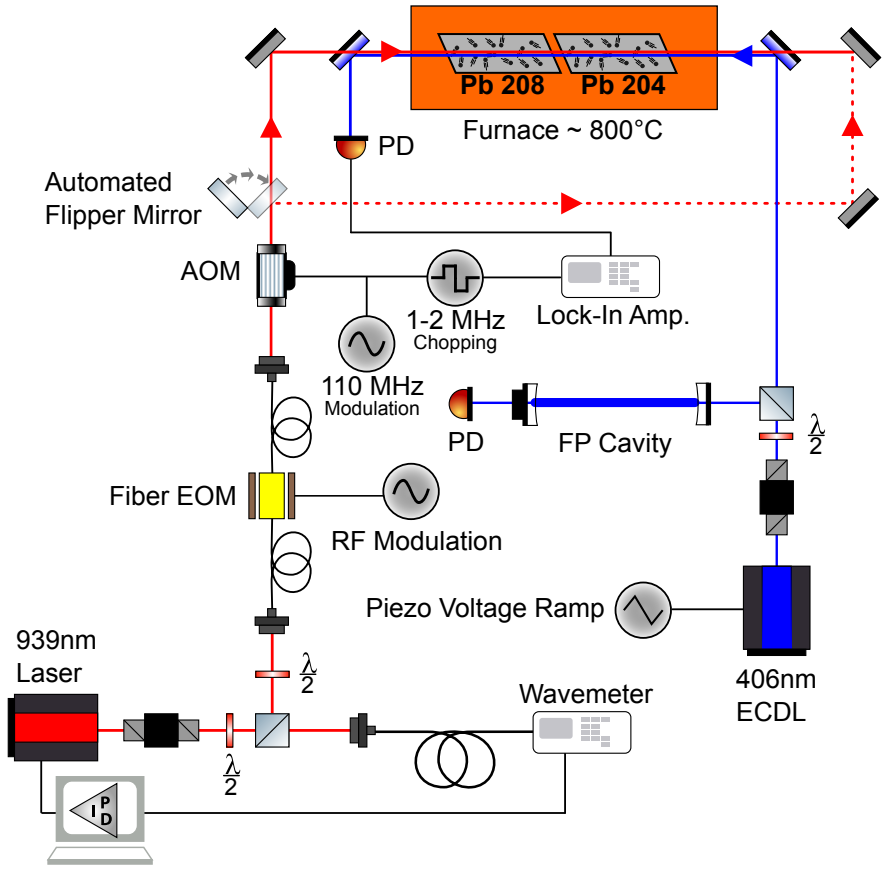


Figure 1: Diagram of the experimental apparatus. The 939 nm pump beam passes through a fiber EOM to generate sidebands and an AOM for lock-in detection, then overlaps with the scanning 406 nm probe beam inside an evacuated furnace containing Pb vapor cells.

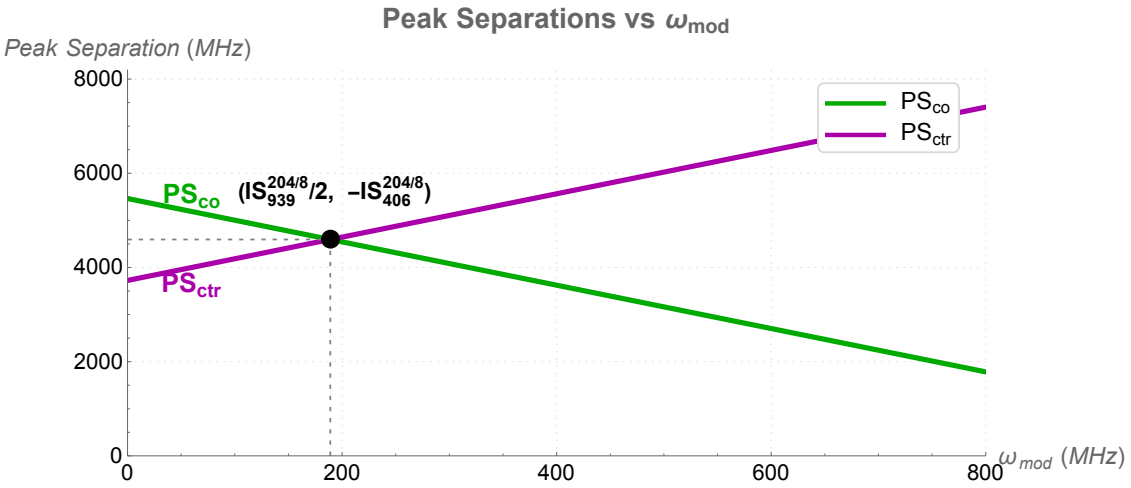


Figure 2: $PS_{co}$ and $PS_{ctr}$ as functions of $\omega_{\mathrm{mod}}$. The two lines intersect at $(IS^{204/8}_{939}/2,\ -IS^{204/8}_{406})$, from which both isotope shifts are read directly.

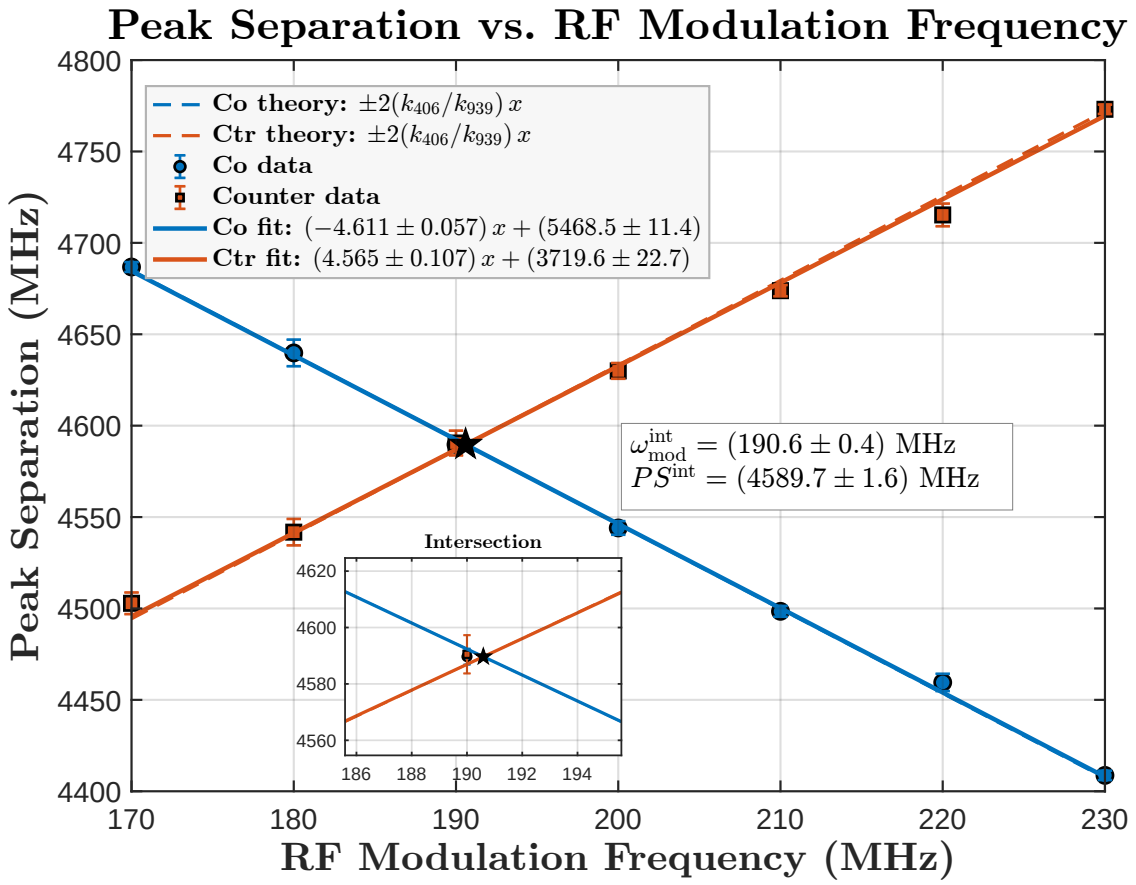


Figure 3: Plot of peak separations vs. modulation frequency for $^{204}$Pb and $^{208}$Pb.

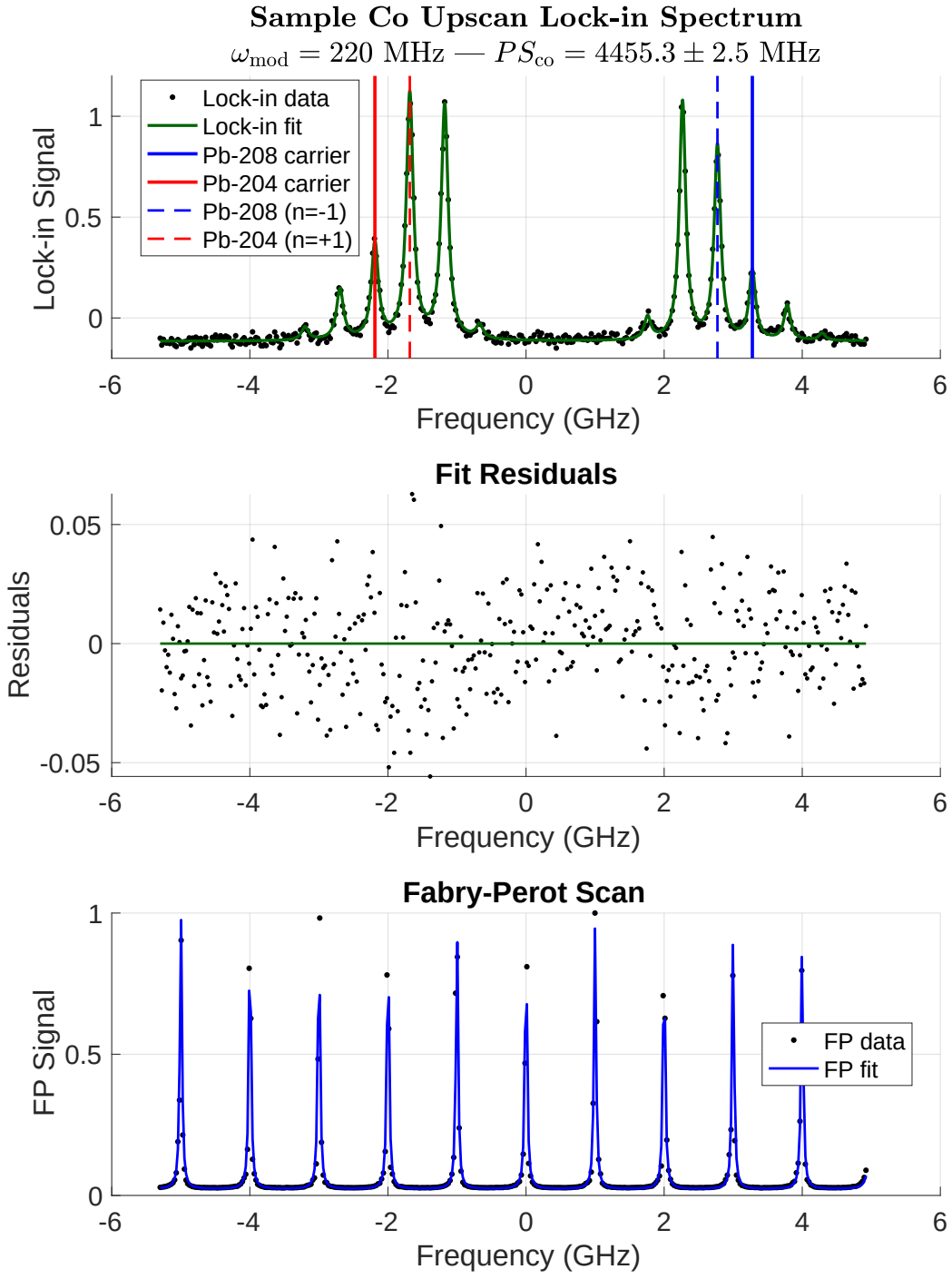


Figure 4: Sample fitted co-aligned upscan at $\omega_{\mathrm{mod}} = 220$ MHz, showing the 14-Lorentzian model (seven sidebands per isotope). The dashed lines mark the relevant $n = \pm 1$ sidebands whose separation defines $PS_{co}$.

# Acknowledgments

Firstly, thank you Tiku for your constant guidance and support over the past few years. I am so lucky to have been part of this wonderful AMO ecosystem that you have seeded here at Williams. Even though my time here has come to an end, I will take this world-class AMO training with me wherever I go — it has been a blessing for me, as it was for the generations of students who came before. Over many decades, your consistent care and effort in cultivating this program has brought together kind and passionate people; I feel this every time I speak with the illustrious alumni of the Majumder Lab, who are now my professors at Williams, my mentors in grad school, and my mentors in industry. Thank you for giving me a chance as a sophomore, for always being available, for being so generous with your time, and for your patience and understanding throughout the writing process. I am excited to see how you continue to grow this community. I'm nervous about living up to those who have come before me, but I'm also excited to see what I can do next.

Thank you John for being not just a mentor, but also a friend. This work was only possible with your tremendous help in the lab. You have a magic touch with lasers — there were times I'd spend hours optimizing the signal and trying to get the laser to run single mode, only for you to step in and get it in an instant. Whatever question I had, you would always write down an equation on the whiteboard right off the dome that explained exactly what was going on. I never stopped learning from you even outside the lab, whether it was the biomechanics of boxing, the darts league, jellied eels, or horse racing. I know you'll do great at Furman — they are so lucky to have you.

Thank you Yazen for always being there next door, for your constant encouragement even when things weren't going my way, and for staying to work with me late into the night in Hopper. I will fondly remember our daily 12:52am dash to SNAR right before they closed for late-night burgers — not to mention our vending machine breaks, which I'm still not sure made us more or less productive. You are so smart, hardworking, and down to earth, and I know you'll be stellar at whatever you choose to pursue.

Theo, thank you for inspiring me with your raw curiosity and passion for science, and for always making time for our Avatar-length calls even while you've been away in China. It has been amazing — and a little disturbing — to learn how much we have in common. We've shared so many laughs over the years; here's to many more.

Thank you Max for your childish energy, positivity, and unwavering friendship. Our many trips to Stewies for ice cream kept me going this year. When I was injured, you took me to the ER, stayed to work with me in my room, and brought me food. You have a big

heart, and I am forever grateful.

Thank you Hiroshi for our Sunday brunch ritual, and for your wisdom on all things pertaining to life. Your humor and groundedness were a blessing when life got chaotic.

Thank you Daniel for leaving the quantum chemistry lab open for all of us to use, for the jazz in the background, and for always being so generous with your time whenever I wanted to talk about something.

Alex, thank you for being one of my closest friends since our freshman year as roommates. I am in awe of your discipline — with sleep, with exercise, with work, and with your commitment to your friends. Thank you for all the runs, swims, and meals that offered respite from work. I know you'll be a brilliant scientist and doctor.

Cole, you inspire me to keep pushing myself to try new things, whether in music, sport, or academics. Your candid questions pushed me to dumb things down and understand them on a deeper level. It's easy to use big words to pretend you know something — you showed me that you only really know something if you can describe it with small ones.

My dear Springstreeters — I could never quite explain how my thesis presentation ended up in our music arrangements Google Drive, but in hindsight it foreshadowed that I would have to sacrifice my senior solo for my thesis. You all were so forgiving despite all the rehearsals I missed. I'm so glad I made it back for our final performance, because singing with you all was the highlight of my week.

Thank you Charlie for being a patient second reader, for your responsiveness, and for setting high standards for me over the many years of physics I have taken with you.

To my all my other friends who have made my time here at Williams so special — thank you.

Finally, thank you Amma and Appa. I would not be here without your love and support over all these years. We may live far apart, but you are always close at heart.

# Contents

# List of Figures

# Chapter 1

# Introduction

## 1.1 The Enterprise of Precision Spectroscopy

Precision spectroscopy is one of the few ways we have to talk to atoms and learn what is really going on inside them. Since Democritus's early hypothesis of their existence, our notion of the atom has evolved dramatically, especially over the past two hundred years—from John Dalton's chemistry of fixed ratios, to Einstein's explanation of Brownian motion, to the discovery of the electron and the nucleus by J.J. Thomson and Ernest Rutherford.

Like a fractal, it seems that the deeper we look, the more structure we find. After Niels Bohr's crucial discovery of quantized electron energy levels, the overwhelming success of the quantum mechanical model, developed by Schrödinger and Heisenberg in the 1920s, has pinned down atomic structure to a remarkable degree.

Despite this success, we only have exact solutions for the electron wavefunction in hydrogen. For all more complex atoms, we must rely on approximations. The only way to know how good those approximations are is to test them at their limits—particularly in complex atoms like lead (Pb).

Electrons in an atom repel each other through the Coulomb interaction, so each electron's motion depends on all the others. Modeling these correlated wavefunctions is challenging. Furthermore, near the nucleus, electrons in heavy atoms move at relativistic speeds, so relativistic effects must also be included. The result is a relativistic quantum many-body problem that cannot be solved exactly. This is where experimental measurements, such as isotope shifts, become important in testing and validating our approximations.

We use Pb because it sits squarely in the regime where modern atomic calculation methods are challenged: Pb is a heavy, multi-valence atom with four valence electrons and strong relativistic effects near the nucleus. It also has four naturally occurring stable isotopes—$^{204}$Pb, $^{206}$Pb, $^{207}$Pb, and $^{208}$Pb—which gives us several independent isotope-shift measurements to cross-compare within the same element.

### 1.1.1 Isotope shifts

Isotope shifts are small differences in transition energies between different isotopes of an element. They arise from two main contributions: the mass shift and the volume shift. The mass shift reflects the finite mass of the nucleus and can be thought of as a small correction due to nuclear motion; it goes as the inverse of the nuclear mass, so for heavy atoms like Pb it is relatively small. The volume shift, on the other hand, arises from the overlap of the s-orbital electron wavefunction with the nucleus: because different isotopes have slightly different nuclear sizes, the s-electrons see slightly different effective potentials, producing an isotope shift proportional to $Z^2$ [4, Section 6.2].

Both of these contributions depend sensitively on the electronic wavefunction near the nucleus, which is exactly the regime where atomic-structure calculations are hardest—and exactly where isotope shifts become an unusually sharp test of atomic theory. The Safronova group at the University of Delaware has made recent progress on this front with a method known as configuration interaction plus all-order (CI + all-order), pushing the accuracy of calculations for heavy, multi-valence systems to the few-percent level [1]. But any such theory is only as good as the experiments that benchmark it, and the experimental side has its own story. Ever since the invention of the laser in the 1960s, coherent, narrow-bandwidth, tunable light sources have let us probe atomic structure with extraordinary resolution—like putting on a new prescription pair of glasses. Precision spectroscopy has, in this sense, become a kind of lie detector for competing atomic models and computational methods, especially in complex systems like Pb where theory is most difficult.

One caveat is worth flagging up front: our experimental method measures only the isotope shifts in transition frequencies—differences between two atomic levels—not the absolute shifts of the individual levels. Even so, those transition shifts contain enough information to probe both atomic structure and nuclear properties. Our own preliminary measurements of the hyperfine constant in $^{207}$Pb have come in a few percent higher than the literature value, and that small discrepancy is what motivates us to independently verify the literature isotope shift values in the first place.

## 1.2 Previous Work

This thesis stands on the shoulders of multiple generations of thesis students that have come before me. Their preparatory work has made this possible. Charles Yang developed the apparatus for Doppler-free spectroscopy [2]. Carter Anderson made the first preliminary isotope shift measurements with the apparatus [5]. Abby Kinny made improvements to the furnace [6]. Past work in the Majumder lab has included high-precision measurements of Stark shifts and related atomic properties in lead, thallium, and indium.

## 1.3 Outline of Thesis

Chapter 2 develops the relevant atomic theory, including the two-step Doppler-free excitation scheme and the Doppler weighting systematic. Chapter 3 lays out the co-counter crossing technique and explains why it is better than the naive single-carrier approach. Chapter 4 describes the experimental apparatus, and Chapter 5 covers data collection. Chapter 6 presents the full analysis pipeline, from Fabry–Pérot frequency calibration through to uncertainty propagation, and Chapter 7 gives our preliminary results for $^{204}\mathrm{Pb}/^{208}\mathrm{Pb}$. Chapter 8 outlines next steps. Appendix A works through the Doppler-weighting systematic in detail; Appendix B tabulates experimental conditions for each dataset.

# Chapter 2

# Atomic Theory

## 2.1 Light Interacting with Atoms

Electrons in atoms occupy discrete energy levels, and they can be excited to higher levels by absorbing a photon of the right energy. The frequencies at which this absorption occurs are called atomic lines. These lines are not perfectly narrow; the Heisenberg uncertainty principle relates the finite lifetime $\tau$ of an excited state to an uncertainty $\Delta E \sim \hbar/\tau$ in its energy, smearing the absorption into a Lorentzian profile of full width $\Gamma \sim 1/\tau$ centered on the nominal line. An atom therefore absorbs photons over a small range of frequencies around the line center.

Excited electrons can also be de-excited by an incoming resonant photon, in a process called stimulated emission. The emitted photon is identical to the stimulating one—same frequency, same direction, same phase. Spontaneous emission, by contrast, releases a photon in a random direction at a rate set by the natural linewidth.

## 2.2 Pb electronic structure

The low-lying energy levels of Pb relevant to our experiment are shown in Fig. 2.1. Our two-step excitation scheme drives the $^3P_1$ and $^3P_2$ states of the ground $6s^2 6p^2$ configuration up to the $^3P_0$ and $^3P_1$ states of the excited $6s^2 6p 7s$ configuration.

Three of Pb's stable isotopes—$^{204}$Pb, $^{206}$Pb, and $^{208}$Pb—have nuclear spin $I = 0$, so there is no coupling between nuclear and electronic angular momentum and therefore no hyperfine structure. The remaining stable isotope, $^{207}$Pb, has $I = \frac{1}{2}$, so each fine-structure level $J$ further splits via the hyperfine interaction into states labeled by $\mathbf{F} = \mathbf{I} + \mathbf{J}$, giving additional spectral structure absent in the even isotopes.

A fuller account of the electron configuration, term-symbol notation, and the $6p^2\,{}^3P_J$ fine-structure manifold is given in Appendix G.

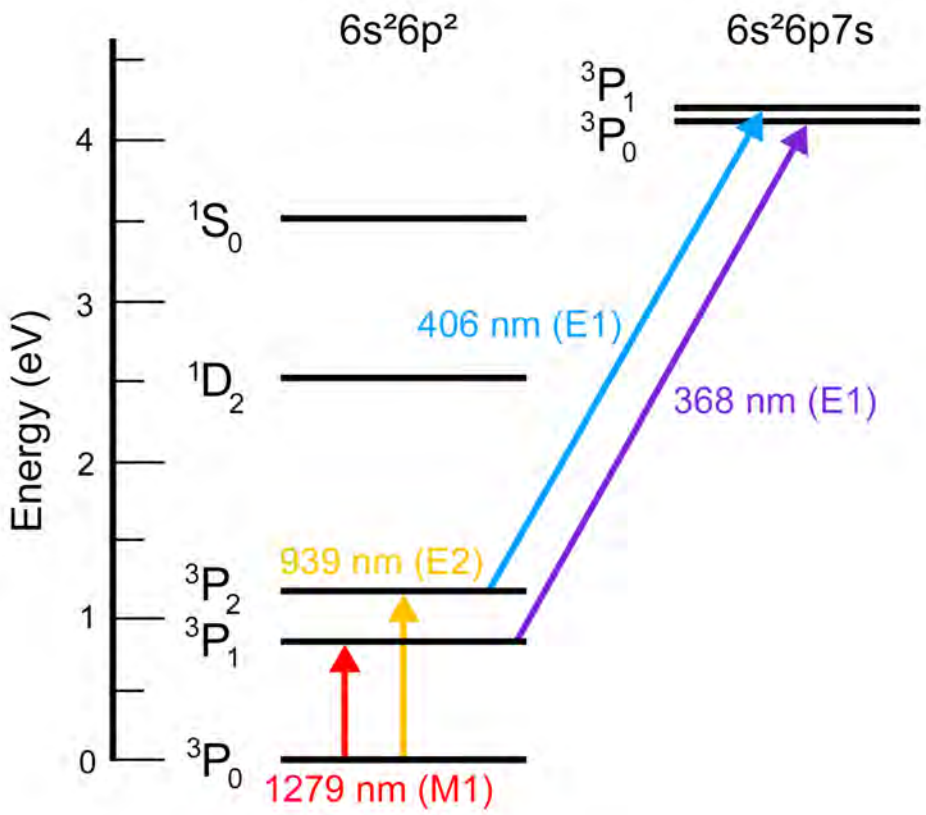


Figure 2.1: Energy level diagram for Pb, reproduced from Robin Wang's thesis [3].

## 2.3 Broadening Mechanisms

The atomic lines we observe in our experiment are broadened by several distinct mechanisms. They can be divided into *inhomogeneous* broadening, in which different atoms experience different shifts and the observed line is a sum over many different sub-populations, and *homogeneous* broadening, in which the line shape of every atom is broadened equally. Table 2.1 lists the order-of-magnitude contributions of each broadening mechanism for the Pb transitions in our experiment, with detailed derivations in Section 2.4 of Carter Anderson's thesis [5] and Section 2.3 of Charles Yang's thesis [2]. Doppler broadening is by far the biggest effect: atoms in the hot furnace are flying around at all different speeds, and because of the Doppler effect each atom sees the laser at a slightly different frequency depending on how fast it is moving. Adding up all those slightly-shifted absorptions smears the line into a broad Gaussian of roughly 1 GHz. Finite-lifetime broadening is a fundamental quantum effect—because an excited state only lives for a finite time $\tau$, the uncertainty principle gives it a small spread in energy, which translates into a natural linewidth of about 15 MHz. Collisional broadening (∼30 MHz) happens when Pb atoms bump into each other mid-absorption, knocking them out of the right velocity class. Pressure broadening (∼1 MHz) is the same idea but from background gas molecules in the cell. Power broadening kicks in when the

laser is so intense that it is actively pushing atoms back and forth between the ground and excited states faster than they can absorb, which washes out the sharpness of the line by about 15 MHz.

| **Broadening Mechanism** | **Type** | **FWHM (MHz)** |
|---|---|---|
| Doppler | Inhomogeneous | 1000 |
| Finite-lifetime | Homogeneous | 15 |
| Pressure | Homogeneous | 1 |
| Collisional | Homogeneous | 30 |
| Power | Homogeneous | 15 |

Table 2.1: Order-of-magnitude FWHM contributions from each broadening mechanism. [5][2]

The observed line shape is the result of all of these mechanisms acting together: a convolution of a Lorentzian profile (from the homogeneous contributions) with a Gaussian profile (from Doppler broadening), known as a *Voigt* profile. Because the Doppler contribution dominates by more than an order of magnitude, the observed raw absorption lines are well approximated by a Gaussian over most of their width.

In 2024, Charles Yang demonstrated a lock-in technique that suppresses the Doppler contribution in our two-step excitation scheme by more than an order of magnitude [2]. An acousto-optic modulator (AOM) chops the first-step laser at MHz-level frequencies, so the velocity class promoted by the first step is sampled by the second step over a time much shorter than the mean time between velocity-changing collisions. The selected velocity class is therefore interrogated before collisional broadening can redistribute it, recovering a Lorentzian-dominated line shape from an otherwise Doppler-dominated spectrum. This technique is what enables the sub-Doppler resolution required for the precision isotope-shift measurement described in the following chapter.

## 2.4 The Doppler Shift

We all know the sound of an ambulance passing by: "weeeee. . . aaaaaaw." The siren sounds higher in pitch as it approaches and lower as it recedes. This is the Doppler effect; wavefronts emitted by the source pile up ahead of its motion and stretch out behind, raising or lowering the apparent frequency accordingly. The same effect applies to atoms moving relative to a laser beam. The velocity of Pb atoms in our furnace follows a Boltzmann distribution, so different atoms experience different Doppler shifts. In the rest frame of an atom moving with velocity $\mathbf{v}$, the laser frequency is shifted by

$$\Delta\omega = -\mathbf{k} \cdot \mathbf{v}, \tag{2.1}$$

where $\mathbf{k}$ is the wavevector of the laser.

To see how this shift connects the two steps of our excitation scheme, consider the first-step transition ($^3P_0 \rightarrow {}^3P_2$) in $^{208}$Pb. Let $\omega_{939}^{208}$ denote the natural resonance frequency of this transition, and let $\omega_{939}^{\text{laser}}$ be the frequency of the 939 nm laser. In general the laser is detuned from the atomic line by

$$\omega_{939}^{\text{laser}} = \omega_{939}^{208} + \Delta\omega_{939}^{\text{laser}}. \tag{2.2}$$

An atom is resonant with the laser only if its motion produces a Doppler shift that exactly cancels this detuning. Setting the laser frequency seen by the atom equal to the natural resonance gives the resonance condition

$$\omega_{939}^{208} = \omega_{939}^{\text{laser}} - \mathbf{k}_{939}^{\text{laser}} \cdot \mathbf{v}, \tag{2.3}$$

or equivalently

$$\Delta\omega_{939}^{\text{laser}} = \mathbf{k}_{939}^{\text{laser}} \cdot \mathbf{v}. \tag{2.4}$$

Due to the narrow linewidth of the first step laser, only atoms in the narrow velocity class satisfying this detuning condition are promoted to the intermediate state.

The second-step laser, at 406 nm, is scanned across frequencies to drive these atoms further. Because only this selected velocity class participates, the second-step transition appears at a Doppler-shifted frequency $\omega_{406}^{\text{res}}$ satisfying

$$\omega_{406}^{208} = \omega_{406}^{\text{res}} - \mathbf{k}_{406}^{\text{laser}} \cdot \mathbf{v}. \tag{2.5}$$

The displacement of the observed 406 nm absorption feature from the true atomic line is therefore

$$\Delta\omega_{406}^{208} = \mathbf{k}_{406}^{\text{laser}} \cdot \mathbf{v}. \tag{2.6}$$

Taking the ratio of the two shifts eliminates the velocity entirely:

$$\frac{\Delta\omega_{406}^{208}}{\Delta\omega_{939}^{\text{laser}}} = \frac{k_{406}^{\text{laser}}}{k_{939}^{\text{laser}}} = \frac{\lambda_{939}^{\text{laser}}}{\lambda_{406}^{\text{laser}}}. \tag{2.7}$$

The shift of the observed second-step resonance from the true atomic line is thus simply the first-step laser detuning scaled by around 2.3, the ratio of the two laser wavelengths.

### 2.4.1 Systematic error from Doppler population weighting

The signal we observe from each isotope peak is proportional to the number of atoms that contribute at each point on the line. In our two-step excitation scheme, the first-step 939 nm laser is locked to a fixed frequency, selecting atoms in a narrow velocity class $v_{\text{sel}}$ from the thermal distribution. As the second-step 406 nm laser scans through the peak, atoms at slightly different velocities contribute at each detuning: an atom detuned by $\Delta\omega$ from the peak center sits at velocity $v_{\text{sel}} + \Delta\omega/k_{406}$. Because the 1D velocity distribution is a Gaussian centered on $v = 0$, the number of available atoms varies across the peak—more atoms on the side closer to $v = 0$, fewer on the side farther away. This asymmetric weighting pulls the apparent peak center toward the natural resonance frequency.

**Why a product, not a convolution.** In single-step absorption spectroscopy, the observed lineshape is the *convolution* of the Lorentzian natural linewidth with the Gaussian Doppler distribution—every atom in the Maxwell–Boltzmann distribution contributes at its own Doppler-shifted frequency, and integrating over velocities gives the well-known Voigt profile. Our two-step experiment is fundamentally different: the first-step laser already preselects a narrow velocity class, so the integration over velocities is effectively performed by the experiment itself rather than by us. The Gaussian thermal distribution then enters as a *population weight* on the selected velocity class—the number of atoms at the velocity corresponding to each point on the Lorentzian follows the Maxwell–Boltzmann distribution—rather than as an integration kernel. The appropriate model is therefore the product

$$S(\omega) = L(\omega - \omega_L)\, W(\omega), \tag{2.8}$$

not the convolution $L * W$.

The closed-form peak-shift formula derived below (Eq. (2.15)) additionally requires that the Lorentzian be narrow compared to the Gaussian, $\gamma_L \ll \sigma$, so that $W(\omega)$ varies only slowly across one Lorentzian width and the correction is well-approximated by the leading-order Gaussian gradient. This condition is comfortably satisfied in our experiment: for the first-step transition, $\gamma_L \approx 40\,\mathrm{MHz}$ sits against a Doppler width $\sigma \approx 525\,\mathrm{MHz}$, giving $\gamma_L/\sigma \approx 0.08$.

Note that this is distinct from the Gaussian broadening due to velocity-changing collisions described, e.g., in Ref. [2]. Collisional broadening randomises the atomic velocity *during* the measurement, which *does* produce a convolution. Here the atoms have fixed velocities set by the thermal distribution, and the Gaussian acts only as a static population weight. The atoms don't have time to thermalize since we are using a lock-in technique that samples them much faster than the characteristic time between collisions.

**Setup.** Each peak has the Lorentzian form

$$L(x) = \frac{\gamma_L^2}{x^2 + \gamma_L^2}, \tag{2.9}$$

where $x$ is the frequency offset from the peak center and $\gamma_L$ is the half width at half maximum. The thermal envelope is a Gaussian centered on the second-step atomic resonance $\omega_a$:

$$W(\omega) = \exp\left[-\frac{(\omega - \omega_a)^2}{2\sigma^2}\right], \qquad \sigma = k_{406}\sqrt{k_B T/m}, \tag{2.10}$$

where $\sigma$ is the 1D Doppler width at 406 nm and $m$ is the isotope mass. For the 939 nm transition in $^{208}$Pb at 800°C, the corresponding Gaussian Doppler profile has a full width at half maximum

$$\mathrm{FWHM}_G = 2\sqrt{2\ln 2}\,\sigma \approx 520\ \mathrm{MHz}. \tag{2.11}$$

The Lorentzian is centered at $\omega_L = \omega_a + \delta$, where $\delta = k_{406} v_{\mathrm{sel}}$ is the Doppler shift of the selected velocity class. If $v_{\mathrm{sel}} = 0$ (first-step laser tuned exactly to the atomic resonance), then

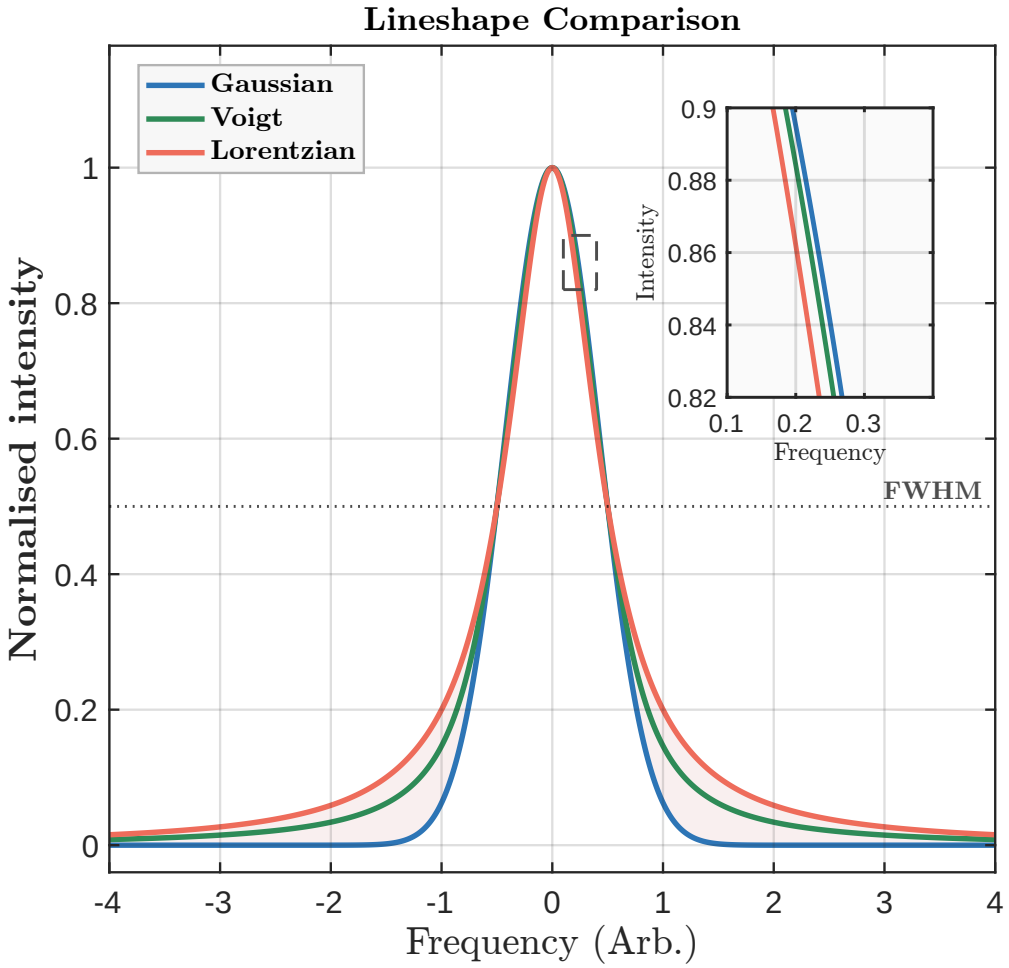


Figure 2.2: Comparison of Gaussian, Lorentzian and Voigt profiles.

$\delta = 0$, the Lorentzian and Gaussian share the same center, and the product is symmetric—no bias. For $\delta \neq 0$, the Gaussian falls off faster on the side of the Lorentzian that is farther from $\omega_a$, and the fitted peak is pulled toward $\omega_a$.

**Deriving the peak shift.** Let $u = \omega - \omega_L$ be the offset from the true Lorentzian center. Then $\omega - \omega_a = u + \delta$ and

$$S(u) = \frac{\gamma_L^2}{u^2 + \gamma_L^2} \exp\left[-\frac{(u+\delta)^2}{2\sigma^2}\right]. \tag{2.12}$$

The apparent peak sits where $dS/du = 0$. Working with $\ln S$ separates the two factors:

$$\frac{d \ln S}{du} = -\frac{2u}{u^2 + \gamma_L^2} - \frac{u + \delta}{\sigma^2} = 0. \tag{2.13}$$

We expect the shift $|u|$ to be small compared to both $\gamma_L$ and $|\delta|$, so we drop $u^2$ in the left denominator and $u$ in the right numerator:

$$\frac{2u}{\gamma_L^2} \approx -\frac{\delta}{\sigma^2}. \tag{2.14}$$

Solving for $u$:

$$\boxed{u \;\approx\; -\frac{\gamma_L^2}{2\sigma^2}\,\delta.} \tag{2.15}$$

The negative sign confirms the physical picture: the apparent peak is pulled away from the Lorentzian center, toward the Gaussian center $\omega_a$.

The approximation requires $|u| \ll \gamma_L$ and $|u| \ll |\delta|$. From Eq. (2.15):

$$\frac{|u|}{\gamma_L} \approx \frac{\gamma_L|\delta|}{2\sigma^2}, \qquad \frac{|u|}{|\delta|} \approx \frac{\gamma_L^2}{2\sigma^2}. \tag{2.16}$$

Both ratios are much less than 1 provided $\gamma_L \ll \sigma$, which holds in our experiment ($\gamma_L/\sigma \approx 75/1700 \approx 0.04$) and $|\delta|$ is at most of order $\sigma$.

**Maximum single-peak bias.** The bias grows linearly with $\delta$, but at $|\delta| \gg \sigma$ there are essentially no atoms in the selected velocity class and no peak to fit. The largest meaningful bias occurs around $|\delta| \sim \sigma$:

$$|u|_{\max} \approx \frac{\gamma_L^2}{2\sigma}. \tag{2.17}$$

For our experiment, $\gamma_L \approx 40\,\text{MHz}$ (HWHM of the observed first-step Lorentzian, corresponding to a $\sim 80\,\text{MHz}$ FWHM), and the Doppler-broadened raw absorption profile at 939 nm has a FWHM of $\sim 525\,\text{MHz}$, giving $\sigma = \text{FWHM}/(2\sqrt{2\ln 2}) \approx 525\,\text{MHz}/2.355 \approx 223\,\text{MHz}$ at $T \approx 1123\,\text{K}$ (850 °C). Substituting:

$$|u|_{\max} \approx \frac{(40\text{ MHz})^2}{2 \times 223\text{ MHz}} \approx 3.6\,\text{MHz}. \tag{2.18}$$

The Gaussian is so much wider than the Lorentzian that it varies only slowly across each peak, keeping the single-peak bias small. In practice we extract peak centers by fitting a symmetric Lorentzian to the data, which does not perfectly follow the skewed shape of $S(\omega)$, so the true fitted-center bias may differ from the estimate above by a factor of two or so—but it remains in the few-MHz range.

When we take the peak separation between two isotopes, this single-peak bias largely cancels—but not exactly, because $^{204}$Pb and $^{208}$Pb have slightly different masses and therefore slightly different Doppler widths. The residual at the crossing point works out to $\sim 33\,\text{kHz}$, well below our current statistical uncertainty. The full derivation is given in Appendix C (Section C.3).

# Chapter 3

# Experimental Methods

## 3.1 The Naive Approach to Measuring Isotope Shifts

The simplest way to extracting both isotope shifts involves using a single laser frequency for the first-step transition, with no modulation. By placing the carrier somewhere between the $^{208}$Pb and $^{204}$Pb atomic lines and recording the resulting 406 nm peak positions in both the co- and counter-aligned beam geometries, one obtains four peaks whose sum and difference yield the two isotope shifts directly.

**Velocity selection.** Because the thermal velocity distribution of the atoms in the vapor cell is broad, the first-step laser addresses a different velocity class of each isotope simultaneously. $^{208}$Pb atoms with velocity $v_{208} = (\omega_{939}^{\text{laser}} - 0)/k_{939}^{\text{laser}}$ are resonant with the laser, as are $^{204}$Pb atoms with velocity $v_{204} = (\omega_{939}^{\text{laser}} - IS_{939}^{204/8})/k_{939}^{\text{laser}}$. Each velocity class produces a single peak in the 406 nm spectrum, Doppler-shifted from its respective atomic transition by the ratio $k_{406}^{\text{laser}}/k_{939}^{\text{laser}}$ (derived in Section 2.4). The sign of this shift flips between co- and counter-alignment.

**Notation and conventions.** We place the $^{208}$Pb line at zero frequency in both the 939 nm and 406 nm spectra. The first-step isotope shift is then

$$IS_{939}^{204/8} = \omega_{204}^{\text{atom},939} - \omega_{208}^{\text{atom},939} > 0, \tag{3.1}$$

and the second-step isotope shift is

$$IS_{406}^{204/8} = \omega_{204}^{\text{atom},406} - \omega_{208}^{\text{atom},406} < 0, \tag{3.2}$$

where $IS_{406}^{204/8}$ is negative because the ordering of the two isotope levels reverses between the first and second transitions. The laser carrier frequency is given by

$$\omega_{939}^{\text{laser}} = \frac{IS_{939}^{204/8}}{2} + \omega_{\text{offset}}, \tag{3.3}$$

so that $\omega_{\text{offset}} = 0$ corresponds to the carrier sitting exactly midway between the two isotope lines. In practice, the lock point is set empirically — for example, by tuning the laser until the two isotope peaks have approximately equal heights — and the residual offset $\omega_{\text{offset}}$ is unknown a priori (see Fig. 3.1).

**Peak positions in the 406 nm spectrum.** Applying the Doppler relation derived in Section 2.4 to each isotope and beam direction:

$$\omega_{co}^{208} = 0 + \frac{k_{406}^{\text{laser}}}{k_{939}^{\text{laser}}}\,\omega_{939}^{\text{laser}} \tag{3.4}$$

$$\omega_{ctr}^{208} = 0 - \frac{k_{406}^{\text{laser}}}{k_{939}^{\text{laser}}}\,\omega_{939}^{\text{laser}} \tag{3.5}$$

$$\omega_{co}^{204} = IS_{406}^{204/8} + \frac{k_{406}^{\text{laser}}}{k_{939}^{\text{laser}}}\left(\omega_{939}^{\text{laser}} - IS_{939}^{204/8}\right) \tag{3.6}$$

$$\omega_{ctr}^{204} = IS_{406}^{204/8} - \frac{k_{406}^{\text{laser}}}{k_{939}^{\text{laser}}}\left(\omega_{939}^{\text{laser}} - IS_{939}^{204/8}\right) \tag{3.7}$$

Each frequency is constructed from the parent atomic line position plus (or minus) the Doppler-scaled detuning of the laser carrier from that line. Co- and counter-alignment appear with opposite signs of the Doppler-scaled detuning. The four peaks form two pairs: the co-aligned 208/204 pair, and the counter-aligned 208/204 pair (see Fig. 3.2).

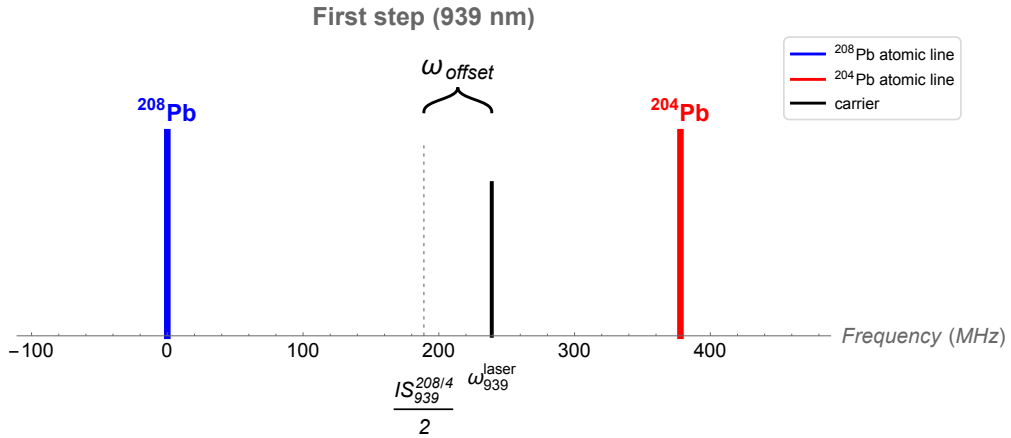


Figure 3.1: First-step laser carrier relative to the $^{208}$Pb and $^{204}$Pb atomic lines, for $\omega_{\text{offset}} = 50\,\text{MHz}$.

**Peak separations.** Define the peak separations for each alignment

$$PS_{co} = \omega_{co}^{208} - \omega_{co}^{204}, \tag{3.8}$$

$$PS_{ctr} = \omega_{ctr}^{208} - \omega_{ctr}^{204}. \tag{3.9}$$

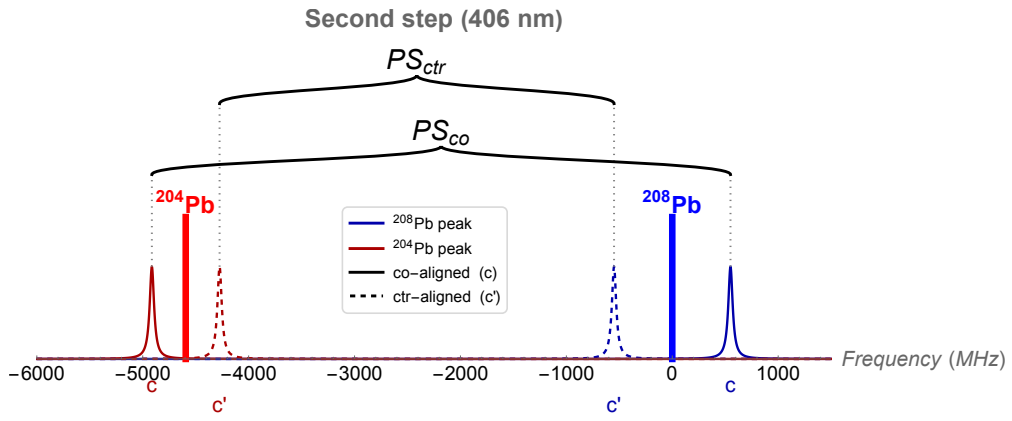


Figure 3.2: Second-step (406 nm) spectrum showing the two co-aligned and two counter-aligned peaks, for $\omega_{\text{offset}} = 50\,\text{MHz}$.

Substituting and simplifying:

$$PS_{co} = \frac{k_{406}^{\text{laser}}}{k_{939}^{\text{laser}}} IS_{939}^{204/8} - IS_{406}^{204/8} \tag{3.10}$$

$$PS_{ctr} = -\frac{k_{406}^{\text{laser}}}{k_{939}^{\text{laser}}} IS_{939}^{204/8} - IS_{406}^{204/8} \tag{3.11}$$

Both peak separations depend only on the two isotope shifts and the known wavevector ratio. The laser offset $\omega_{\text{offset}}$ has dropped out exactly: because the two peaks within a single alignment share the same Doppler scaling of $\omega_{939}^{\text{laser}}$, that common term cancels when the difference is taken. The technique therefore does not require precise knowledge of where the laser sits between the two atomic lines, only that it lies within range of both.

**Inverting for the isotope shifts.** Subtracting Eq. (3.11) from Eq. (3.10) isolates $IS_{939}^{204/8}$, while adding them isolates $IS_{406}^{204/8}$:

$$\boxed{IS_{939}^{204/8} = \frac{k_{939}^{\text{laser}}}{2\,k_{406}^{\text{laser}}}\left(PS_{co} - PS_{ctr}\right)} \tag{3.12}$$

$$\boxed{IS_{406}^{204/8} = -\tfrac{1}{2}\left(PS_{co} + PS_{ctr}\right)} \tag{3.13}$$

A single pair of co- and counter-aligned scans, in principle, fully determines both isotope shifts.

## 3.2 Co- and Counter-Crossing Approach

A more precise method for measuring the isotope shifts locks the first-step laser near the midpoint of the two atomic lines and adds first-order sidebands using a fiber-based electro-

optic modulator (EOM). The carrier and the two sidebands address different velocity classes of the atoms simultaneously, producing a structured pattern of peaks in the second-step (406 nm) spectrum. By scanning $\omega_{\text{mod}}$ over a range near half the first-step isotope shift and recording the peak separations for the co- and counter-alignments, we obtain a pair of straight lines whose intersection yields both isotope shifts directly. As shown below, the result is insensitive to the precise lock point of the laser: the offset $\omega_{\text{offset}}$ cancels exactly in the final expressions.

**Sideband notation.** The first-step laser is locked at the carrier frequency $\omega_{939}^{\text{laser}}$ defined in Eq. (3.3). The EOM produces two first-order sidebands at $\omega_{939}^{\text{laser}} \pm \omega_{\text{mod}}$. The detuning of each component (carrier or sideband) from each isotope's atomic line is

$$\Delta\omega_{939}^{208}(n) = \frac{IS_{939}^{204/8}}{2} + \omega_{\text{offset}} + n\,\omega_{\text{mod}} \tag{3.14}$$

$$\Delta\omega_{939}^{204}(n) = -\frac{IS_{939}^{204/8}}{2} + \omega_{\text{offset}} + n\,\omega_{\text{mod}} \tag{3.15}$$

where $n \in \{-1, 0, +1\}$ labels the lower sideband, carrier, and upper sideband respectively (Fig. 3.3).

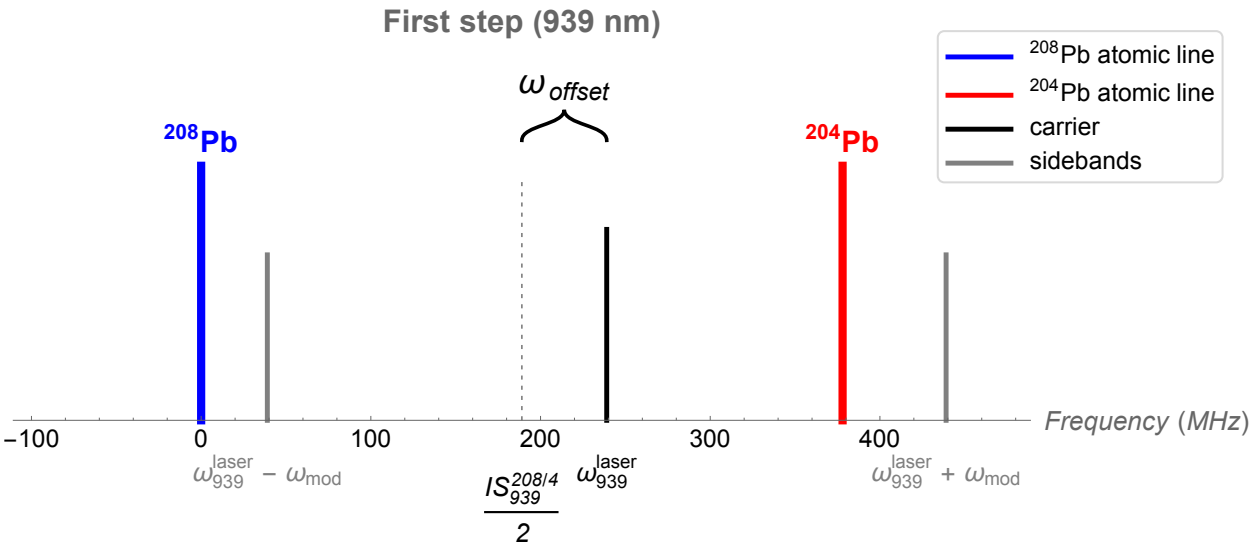


Figure 3.3: First-step laser carrier and sidebands relative to the $^{208}$Pb and $^{204}$Pb atomic lines, for $\omega_{\text{mod}} = 200\,\text{MHz} > IS_{939}^{204/8}/2$.

**The 406 nm spectrum.** Because all three first-step components fall within the Doppler-broadened velocity distribution of each isotope, the 406 nm spectrum exhibits six peaks per alignment: three for each isotope. Applying the same Doppler relation as in the previous

section to each sideband, the observed peak positions are

$$\omega_{co}^{208}(n) = 0 + \frac{k_{406}^{\text{laser}}}{k_{939}^{\text{laser}}} \Delta\omega_{939}^{208}(n) \tag{3.16}$$

$$\omega_{ctr}^{208}(n) = 0 - \frac{k_{406}^{\text{laser}}}{k_{939}^{\text{laser}}} \Delta\omega_{939}^{208}(n) \tag{3.17}$$

$$\omega_{co}^{204}(n) = IS_{406}^{204/8} + \frac{k_{406}^{\text{laser}}}{k_{939}^{\text{laser}}} \Delta\omega_{939}^{204}(n) \tag{3.18}$$

$$\omega_{ctr}^{204}(n) = IS_{406}^{204/8} - \frac{k_{406}^{\text{laser}}}{k_{939}^{\text{laser}}} \Delta\omega_{939}^{204}(n) \tag{3.19}$$

Figure 3.4 shows the resulting twelve peaks (six per alignment) for $\omega_{\text{offset}} = 50\,\text{MHz}$ and $\omega_{\text{mod}} = 200\,\text{MHz}$, with $\omega_{\text{mod}}$ a little larger than $IS_{939}^{204/8}/2$.

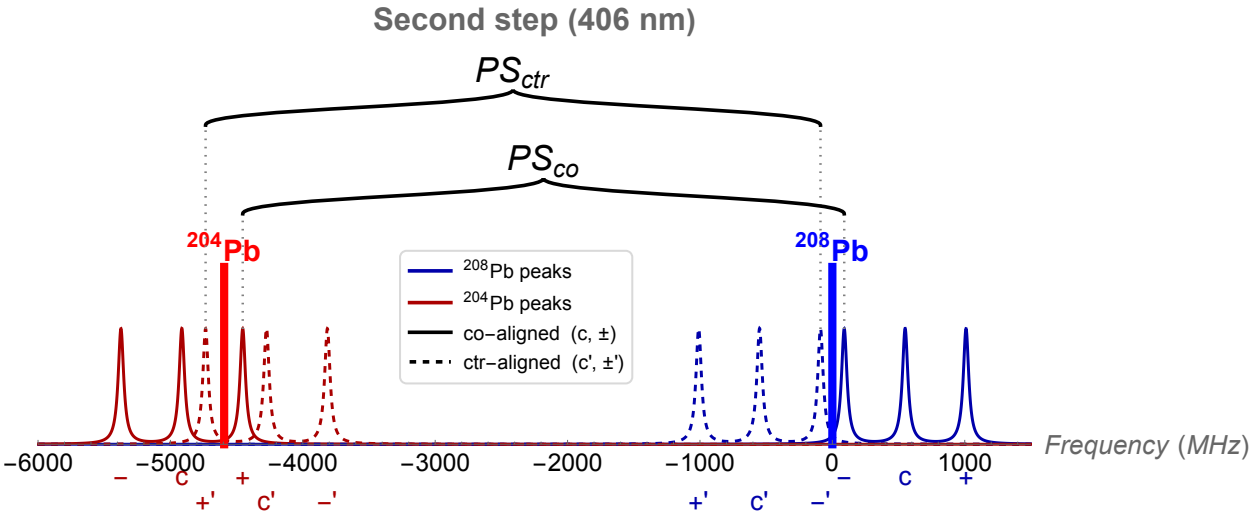


Figure 3.4: Simulation of second-step (406 nm) spectrum showing the six co-aligned and six counter-aligned peaks, for $\omega_{\text{offset}} = 50\,\text{MHz}$ and $\omega_{\text{mod}} = 200\,\text{MHz} > IS_{939}^{204/8}/2$. In reality, the peaks are not all the same height due to the Gaussian 1D Boltzmann distribution of atoms that modulates them.

**Defining the peak separations.** We define $PS_{co}$ as the separation between the innermost peaks of the co-aligned spectrum and $PS_{ctr}$ as the separation between the outermost peaks of the counter-aligned spectrum. These pairs are the ones whose underlying sidebands address the centers of the two atomic resonances:

$$PS_{co} = \omega_{co}^{208}(-1) - \omega_{co}^{204}(+1) \tag{3.20}$$

$$PS_{ctr} = \omega_{ctr}^{208}(-1) - \omega_{ctr}^{204}(+1) \tag{3.21}$$

**Co-aligned peak separation.**

$$\begin{aligned} PS_{co} &= \omega_{co}^{208}(-1) - \omega_{co}^{204}(+1) \\ &= \frac{k_{406}^{\text{laser}}}{k_{939}^{\text{laser}}}\left[\frac{IS_{939}^{204/8}}{2} + \omega_{\text{offset}} - \omega_{\text{mod}}\right] \\ &\quad - IS_{406}^{204/8} - \frac{k_{406}^{\text{laser}}}{k_{939}^{\text{laser}}}\left[-\frac{IS_{939}^{204/8}}{2} + \omega_{\text{offset}} + \omega_{\text{mod}}\right] \\ &= \frac{k_{406}^{\text{laser}}}{k_{939}^{\text{laser}}}\Big[IS_{939}^{204/8} - 2\,\omega_{\text{mod}}\Big] - IS_{406}^{204/8} \end{aligned} \tag{3.22}$$

**Counter-aligned peak separation.**

$$\begin{aligned} PS_{ctr} &= \omega_{ctr}^{208}(-1) - \omega_{ctr}^{204}(+1) \\ &= -\frac{k_{406}^{\text{laser}}}{k_{939}^{\text{laser}}}\left[\frac{IS_{939}^{204/8}}{2} + \omega_{\text{offset}} - \omega_{\text{mod}}\right] \\ &\quad - IS_{406}^{204/8} + \frac{k_{406}^{\text{laser}}}{k_{939}^{\text{laser}}}\left[-\frac{IS_{939}^{204/8}}{2} + \omega_{\text{offset}} + \omega_{\text{mod}}\right] \\ &= -\frac{k_{406}^{\text{laser}}}{k_{939}^{\text{laser}}}\Big[IS_{939}^{204/8} - 2\,\omega_{\text{mod}}\Big] - IS_{406}^{204/8} \end{aligned} \tag{3.23}$$

In both expressions the $\omega_{\text{offset}}$ terms cancel exactly. This cancellation is the central feature of the technique: because the lower and upper sidebands carry opposite signs of $n$, the common laser-offset shift drops out of the difference, while the isotope-shift content survives. As in the direct method, the measurement does not require precise knowledge of the lock point.

**Inverting to extract the isotope shifts.** Subtracting Eq. (3.23) from Eq. (3.22):

$$PS_{co} - PS_{ctr} = 2\,\frac{k_{406}^{\text{laser}}}{k_{939}^{\text{laser}}}\Big[IS_{939}^{204/8} - 2\,\omega_{\text{mod}}\Big] \tag{3.24}$$

$$\boxed{IS_{939}^{204/8} = \frac{k_{939}^{\text{laser}}}{2\,k_{406}^{\text{laser}}}\big(PS_{co} - PS_{ctr}\big) + 2\,\omega_{\text{mod}}} \tag{3.25}$$

Adding Eqs. (3.22) and (3.23):

$$PS_{co} + PS_{ctr} = -2\,IS_{406}^{204/8} \tag{3.26}$$

$$\boxed{IS_{406}^{204/8} = -\frac{1}{2}\big(PS_{co} + PS_{ctr}\big)} \tag{3.27}$$

Plotted as functions of $\omega_{\mathrm{mod}}$, $PS_{co}$ and $PS_{ctr}$ are straight lines of equal magnitude and opposite slope that cross at

$$\left(\omega_{\mathrm{mod}},\, PS\right) = \left(\frac{IS_{939}^{204/8}}{2},\, -IS_{406}^{204/8}\right). \tag{3.28}$$

Reading off the intersection therefore yields both isotope shifts simultaneously. Because $IS_{406}^{204/8} < 0$ in our sign convention, the $y$-coordinate of the intersection is positive (Fig. 3.5).

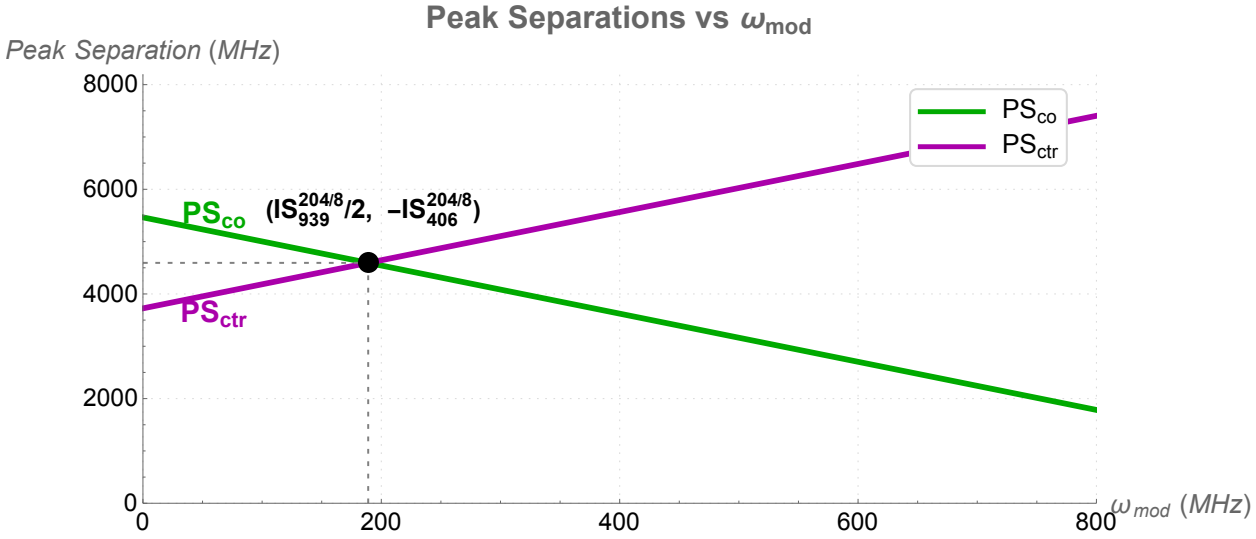


Figure 3.5: $PS_{co}$ and $PS_{ctr}$ as functions of $\omega_{\mathrm{mod}}$. The two lines intersect at $\left(IS_{939}^{204/8}/2,\, -IS_{406}^{204/8}\right)$, from which both isotope shifts can be read off directly.

## 3.3 Why the co- and counter-crossing method is better

The naive method extracts both isotope shifts from just four peak-center fits and provides no internal way to detect or absorb systematic errors. The crossing technique addresses these weaknesses on five fronts.

*(i) Many points instead of four.* In the naive method the precision of $IS_{939}^{204/8}$ and $IS_{406}^{204/8}$ is set by the precision of single peak-center fits, and the only way to improve it is to repeat the measurement and average. The crossing method instead samples $PS_{co}$ and $PS_{ctr}$ at many values of $\omega_{\mathrm{mod}}$ and fits two straight lines through the data. The slope and intercept of each line are determined jointly by every data point, so the fit uncertainty per scan enters the final result as $\sim 1/\sqrt{N}$, where N is the number of $\omega_{mod}$ values sampled, rather than directly. Doubling N roughly halves the uncertainty on the crossing-point coordinates, and unlike repeated scans of the same point, sampling along $\omega_{\mathrm{mod}}$ also tests the linear model.

*(ii) Bias cancellation at the intersection point.* The recorded peaks are not pure Lorentzians but the product of the atomic Lorentzian and a Boltzmann velocity weighting. When the

selected velocity class is far from $v = 0$, the weighting is asymmetric across the peak and biases the fitted center toward $v = 0$. This bias is present on every scan and is not removed by averaging.

The crossing method exploits a special operating point: at $\omega_{\text{mod}} = IS_{939}^{204/8}/2$, the inner co-aligned sidebands sit at the same distance from their respective atomic lines, so they select the same velocity class in both isotopes. The Boltzmann weighting across the two peaks is then nearly identical, and the peak-center biases cancel almost exactly in the sum-and- difference combinations. Even if measurements at the exact crossing are impractical because the Lorentzians from neighboring sidebands begin to overlap, the two linear fits extrapolate to it cleanly, and the extrapolated crossing point is immune to this systematic. (There is a small correction below the level of our noise; the 1D Doppler widths between the isotopes are slightly different since the width scales as $1/\sqrt{m}$ and $^{204}$Pb and $^{208}$Pb have a $\sim 2\%$ mass difference.)

*(iii) Built-in self-consistency check.* The naive method has exactly enough information to determine the two isotope shifts and no degrees of freedom left over to flag problems. Any unaccounted-for systematic appears simply as a wrong answer. The crossing method expects $PS_{co}$ and $PS_{ctr}$ to be linear in $\omega_{\text{mod}}$, with equal magnitude and opposite slope. Any curvature, slope mismatch, or a trend in fit residuals is a direct sign of systematics. Indeed, this was how we identified the Doppler-weighting bias which gave us a slope 2% off from the wavelength ratio we expected.

*(iv) RF-referenced frequency axis.* In the naive method, the conversion from peak separation to $IS_{939}^{204/8}$ depends on the wavevector ratio $k_{939}^{\text{laser}}/k_{406}^{\text{laser}}$, which is set by laser wavelengths and inherits whatever uncertainties those wavelengths carry. In the crossing method, the $x$-coordinate of the crossing is exactly $IS_{939}^{204/8}/2 = \omega_{\text{mod}}$, and $\omega_{\text{mod}}$ is the EOM drive frequency, set by an RF synthesizer locked to a quartz reference. The first-step isotope shift is therefore tied directly to a precisely-known RF frequency and serves as a second frequency ruler, separate from the Fabry Perot peaks.

*(v) Insensitivity to laser drift.* Because $\omega_{\text{offset}}$ cancels exactly in both peak separations (Eqs. (3.22) and (3.23)), slow drifts in the lock point of the first-step laser do not propagate into the result.

In summary, in the co-counter crossing method, the line fit averages over many data points; the crossing point has almost no bias; the linearity check uncovers any systematics; the RF modulation gives an in-situ frequency scale; and the offset cancellation makes the result robust to slow drifts in the laser lock. The naive method has none of these advantages, which is why we adopt the crossing technique for our measurement.

## 3.4 Peak separations with Doppler Weighting Systematic

By the Doppler weighting systematic described in section 2.4.1, the Lorentzian lineshapes get skewed in the direction of the natural resonance. This will naturally affect the peak

separations when applying sidebands that sit at different points on the velocity distribution of Pb isotopes in the ground state. We investigated this systematic by looking at how the change peak separations between the first order sidebands of a single isotope second step spectrum varied with carrier frequency scanned across the resonance of the first step transition. Both simulation and experiment, both corroborating one another.

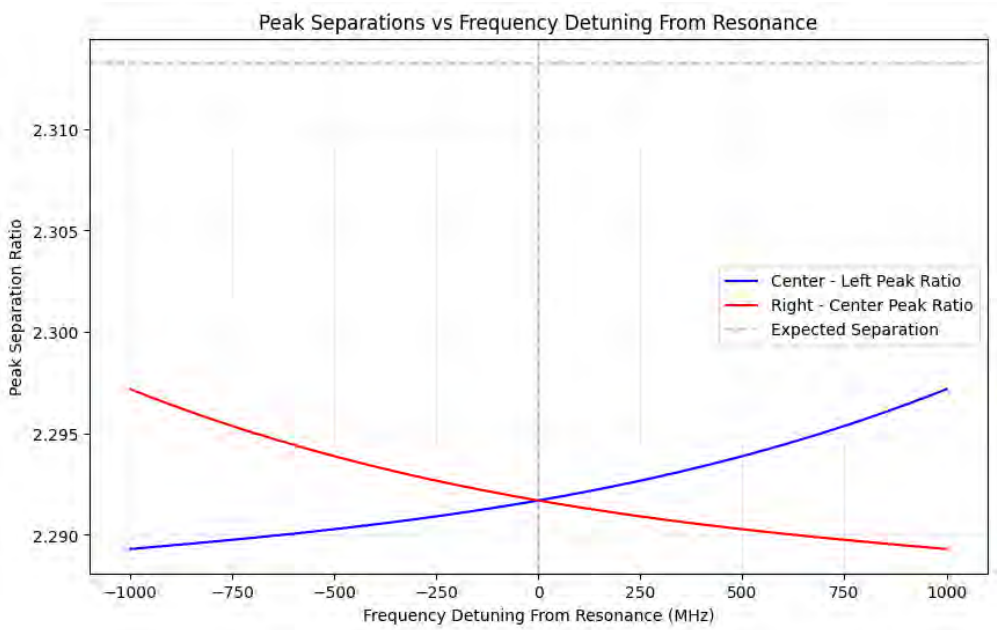


Figure 3.6: Simulation showing the systematic shift in peak separations due to Doppler weighting.

# Chapter 4

# Apparatus

## 4.1 Experimental setup for measuring Pb isotope shifts

We use a Toptica DL Pro 939 nm laser to drive the first-step transition, and a 406 nm external cavity diode laser (ECDL) for the second step. The 939 nm laser is locked to a wavemeter using digital PID feedback. Sidebands are added to the 939 nm beam by a tunable fiber-based electro-optic modulator (EOM), and the beam is chopped by an acousto-optic modulator (AOM) for our lock-in technique. The 406 nm ECDL is scanned across a range of $\sim$10 GHz and monitored using a Fabry–Perot cavity. Pb is a solid at room temperature and pressure—in that form, the atoms interact strongly with their neighbors and form broad band-like electronic states rather than the clean discrete atomic levels we want to probe. To recover the free-atom spectrum, we heat the sample until it produces a vapor. The 406 nm probe and the 939 nm pump beams are then overlapped in quartz vapor cells, which sit inside an evacuated furnace at $\sim$800 °C. The furnace is evacuated to protect the cells from oxidation: in summer 2024 one of our cells developed a leak, oxygen reached the lead inside, and the sample oxidized. A detailed description of each component is given in Carter Anderson's thesis [5].

We made two major modifications to the setup described in Ref. [5]. First, we added a tunable fiber EOM in the path of the 939 nm beam, and second, we replaced the beam splitter that previously divided the 939 nm beam between co- and counter-propagating paths with a motorized flipper mirror. The remaining optics and electronics are unchanged, apart from a few additional lenses to narrow the beam waist inside the vapor cell. The two modifications are described in detail in the next two sections.

## 4.2 Fiber EOM system

The tunable fiber-based electro-optic modulator (EOM) is the key component that enables the co- and counter-crossing technique. We use the Thorlabs LNY1010A phase modulator. The 939 nm carrier sits slightly below the manufacturer's recommended operating range of

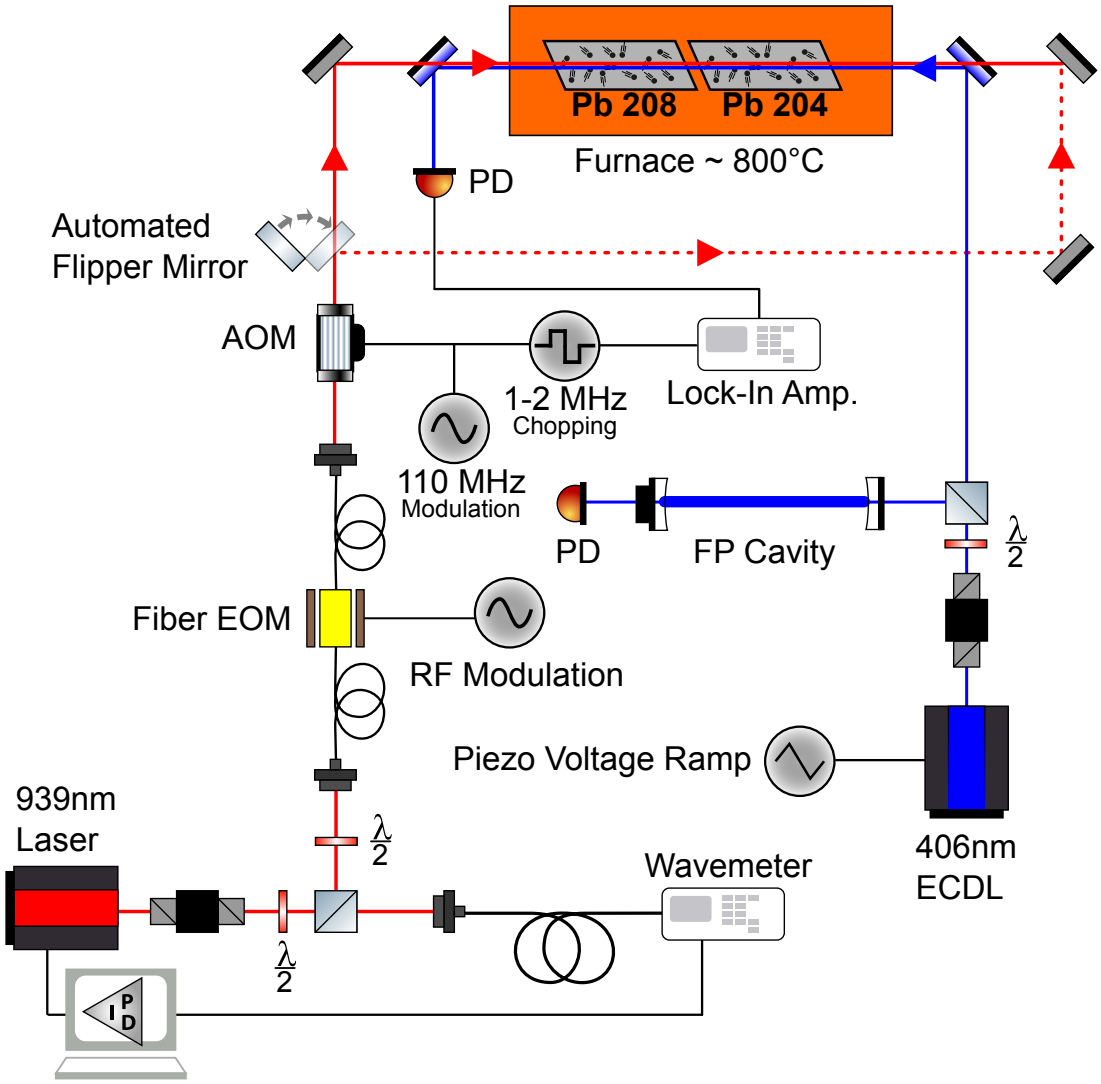


Figure 4.1: Diagram of the experimental apparatus.

1030 nm to 1090 nm [7], but in practice the modulator's performance is more than sufficient for our purposes.

In a phase modulator, an applied electric field linearly changes the refractive index of a lithium niobate crystal (the Pockels effect), which in turn changes the phase accrued by the laser as it passes through the crystal. The Fourier expansion of this time-varying phase breaks the modulated field into discrete frequency components, which appear as sidebands offset from the original carrier frequency. The input polarization must be aligned with the crystal's principal axis for the Pockels effect to act on it [8], so we use a half-wave plate

before the polarization-maintaining input fiber to adjust the polarization.

The advantage of the tunable fiber EOM over a resonant EOM is that it operates over a broad range of modulation frequencies, which is necessary for sweeping $\omega_{\mathrm{mod}}$ across the range of sideband detunings used in our experiment.

**Sideband structure.** Following the derivation in Section 7.10 of Svelto's *Principles of Lasers* [9], consider a monochromatic plane wave entering the EOM,

$$E(t) = E_0\, e^{i\omega_L t}, \tag{4.1}$$

where $\omega_L$ is the carrier (laser) frequency. A sinusoidal modulation voltage at frequency $\omega_{\mathrm{mod}}$ produces a time-dependent phase shift,

$$E(t) = E_0\, e^{i\omega_L t + i\beta\sin(\omega_{\mathrm{mod}} t)}, \tag{4.2}$$

where the modulation depth $\beta$ is set by the RF power driving the EOM. Expanding the modulated phase factor with the Jacobi–Anger identity,

$$e^{i\beta\sin(\omega_{\mathrm{mod}} t)} = \sum_{n=-\infty}^{\infty} J_n(\beta)\, e^{in\omega_{\mathrm{mod}} t}, \tag{4.3}$$

where $J_n(\beta)$ is the $n$th-order Bessel function of the first kind (Fig. 4.2). Bessel functions arise generically in problems with cylindrical symmetry; here they tell us how the input optical power redistributes among the sidebands. Substituting back into the field gives

$$E(t) = E_0 \sum_{n=-\infty}^{\infty} J_n(\beta)\, e^{i(\omega_L + n\omega_{\mathrm{mod}})t}. \tag{4.4}$$

Phase modulation therefore generates an infinite set of sidebands at

$$\omega_n = \omega_L + n\,\omega_{\mathrm{mod}}, \qquad n \in \mathbb{Z}, \tag{4.5}$$

with amplitudes $J_n(\beta)$.

Using the identity $J_{-n}(\beta) = (-1)^n J_n(\beta)$, the field can be written explicitly in terms of upper and lower sidebands. The upper and lower first-order sidebands carry opposite signs, but this phase relationship has no consequence in our experiment because we detect only intensity, which depends on the squared field amplitude.

**Operating point.** We operate at a modulation depth close to $\beta \approx 1.43$, where $J_0(\beta) \approx J_1(\beta)$ and the carrier and each first-order sideband carry approximately equal amplitudes (dotted line in Fig. 4.2). Higher-order sidebands are not completely suppressed at this $\beta$ ($J_2(\beta) \approx 0.35$), so our fitting model accounts for the contribution of second order sidebands although they are not used for the crossing method analysis. Equal amplitudes for the carrier and first-order sidebands are convenient for the data fitting because all three sets of peaks in the second-step spectrum then have comparable heights and signal-to-noise ratios.

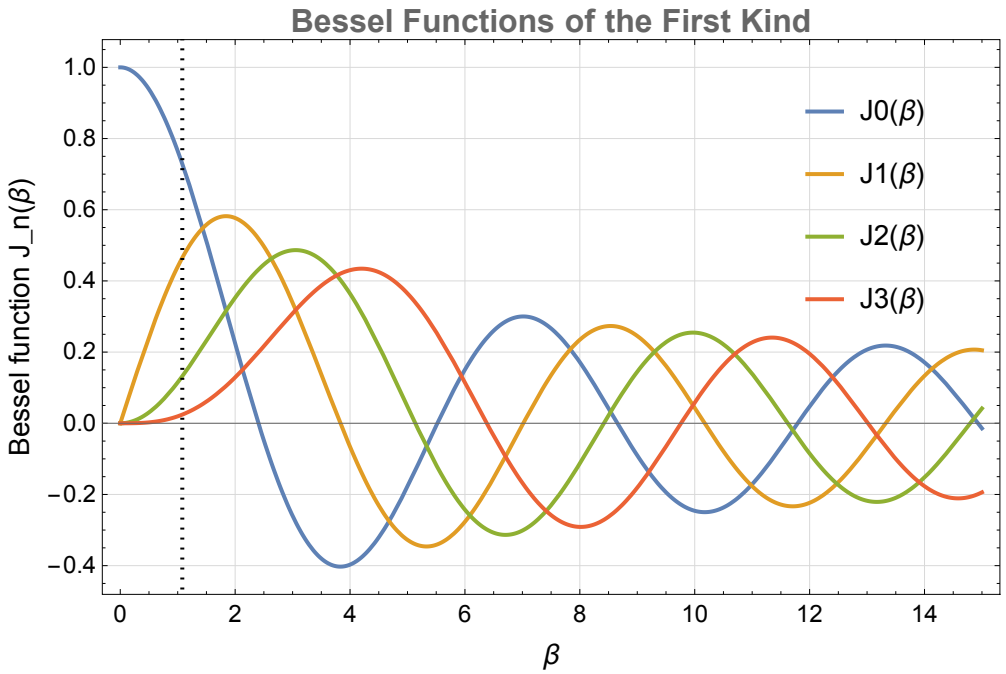


Figure 4.2: The first four Bessel functions of the first kind. The dotted line marks the modulation depth used in our experiment, where $J_0(\beta) \approx J_1(\beta)$.

## 4.3 Motorized flipper mirror

In Carter Anderson's setup, a 50:50 beam splitter divided the 939 nm beam into co- and counter-propagating paths, which were both overlapped with the probe beam simultaneously. We replaced this with a motorized flipper mirror (Thorlabs MFF101) that directs the entire 939 nm beam into one path at a time. Because all of the available pump power now drives a single geometry rather than half going into each, the number of atoms promoted to the intermediate state in that geometry doubles, and the modulated absorption signal observed by the lock-in roughly doubles as well. (The first-step transition is a highly forbidden $E2$ transition, so we are far from saturating it; doubling the pump power gives close to twice the intermediate-state population.)

The flipper has excellent positional repeatability, so re-alignment is not required after each flip. We trigger it from our LabVIEW data collection software with a TTL pulse, configured so that the mirror flips after each scan sequence (a complete pair of up-scan and down-scan, see Table 5.1). Alternating co- and counter-aligned scans on this short timescale rather than collecting all co-scans followed by all counter-scans suppresses systematics from slow drifts — in laser power, vapor-cell temperature, atomic density, or scan-axis calibration — that would otherwise appear as a false offset between $PS_{co}$ and $PS_{ctr}$.

## 4.4 Lock-in detection

We use lock-in detection to extract the small pump-induced absorption signal from the broadband noise floor. The 939 nm pump laser is chopped by an AOM, so any component of the 406 nm absorption that oscillates at the chopping frequency must originate from pump-promoted intermediate-state atoms; all other noise contributions—electrical, acoustic, $1/f$, dark current, ambient light—are rejected. A full description of the technique, including the mathematical treatment and step-by-step simulations, is given in Appendix F.

## 4.5 1279 nm laser locking

### 4.5.1 Show stability with respect to cavity, show line width measurement. Before and after adding thermal isolation.

### 4.5.2 Discuss attempt at locking to Pb vapor cell in small furnace; saw raw absorption dips that were too small so we used cavity lock instead

## 4.6 406 nm Blue laser construction from summer 2024

### 4.6.1 Drawings and blueprints

This External Cavity Diode Laser is based on blueprints from Prof. Charlie Doret [10].

### 4.6.2 FP scans

# Chapter 5

# Data Collection

## 5.1 Experimental sequence

The experimental sequence is as follows. We choose a pair of isotopes—say, $^{204}$Pb and $^{208}$Pb—and scan the 406 nm laser up and down continuously in a linear ramp, with the 939 nm beam overlapped with it in the co-direction, through both Pb vapor cells in series. We add sidebands to the 939 nm beam using the fiber EOM at the lowest frequency in our range of interest.

The LabVIEW program collects data via the DAC on the following channels: the lock-in signal, the 406 nm raw transmission through the Fabry–Pérot cavity, the TTL of the function generator that ramps the 406 nm laser current, and the 406 nm raw transmission through the furnace. The LabVIEW program is configured to automatically send digital pulses to the flipper mirror to switch between co- and counter-alignment by counting the up- and down-scans using the TTL signal. Table 5.1 outlines the order of the up/down, co/counter scans for one experimental cell of data. This sequence is looped until a sufficient number of scans is collected.

| Co-alignment | | | | Counter-alignment | | | |
|---|---|---|---|---|---|---|---|
| Upscan | Downscan | Upscan | Downscan | Upscan | Downscan | Upscan | Downscan |

Table 5.1: Experimental sequence for one cell of data. A motorized flip mirror is used to switch between co- and counter-alignment at the end of each sequence. We loop this until we get sufficient data points. Note that there are two possible experimental sequences; this one, and also one where each alignment starts instead with a downscan. It all depends on the starting position of the motorized flipper mirror since it is toggled by the LabVIEW program, and it doesn't know the initial state.

Instead of simply collecting a long series of co-scans followed by a long series of counter-scans, we alternate between co- and counter-alignment to eliminate the effects of long-term Fabry–Pérot cavity drift, which is crucial for our frequency-axis calibration. See table 5.2 for

a summary of the data collected for $^{204}$Pb and $^{208}$Pb with sideband modulation at various frequencies.

Table 5.2: $^{204}$Pb and $^{208}$Pb data collected at various RF modulation frequencies, taken 17 April 2026.

| $\omega_{mod}$ (MHz) | Co-alignment | | Counter-alignment | | Total |
|---|---|---|---|---|---|
| | Upscans | Downscans | Upscans | Downscans | Scans |
| 160 | 6 | 6 | 7 | 7 | 26 |
| 170 | 6 | 6 | 8 | 7 | 27 |
| 180 | 7 | 7 | 6 | 6 | 26 |
| 190 | 7 | 8 | 6 | 6 | 27 |
| 200 | 6 | 6 | 7 | 8 | 27 |
| 210 | 8 | 7 | 6 | 6 | 27 |
| 220 | 6 | 6 | 7 | 7 | 26 |
| 230 | 6 | 6 | 7 | 8 | 27 |
| **Total** | **58** | **58** | **61** | **62** | **239** |

See figure 5.1 for sample data of a few up- and down-scans collected via the LabVIEW program. The amplitude of the lock-in peaks for the co-direction is twice as large as the counter-direction possibly due to better beam overlap and power. The optical path is different for both geometries so naturally there will be some discrepancies, but future improvements can certainly be made to boost the signal in the counter direction. Note that the raw transmission rises and falls with the current ramp on the laser since the beam intensity increases with current. Later on in our data processing, we will divide the lock-in signal by the raw transmission to normalize it. The TTL will allow us to easily chop up the raw data into up-scans and down-scans for further processing.

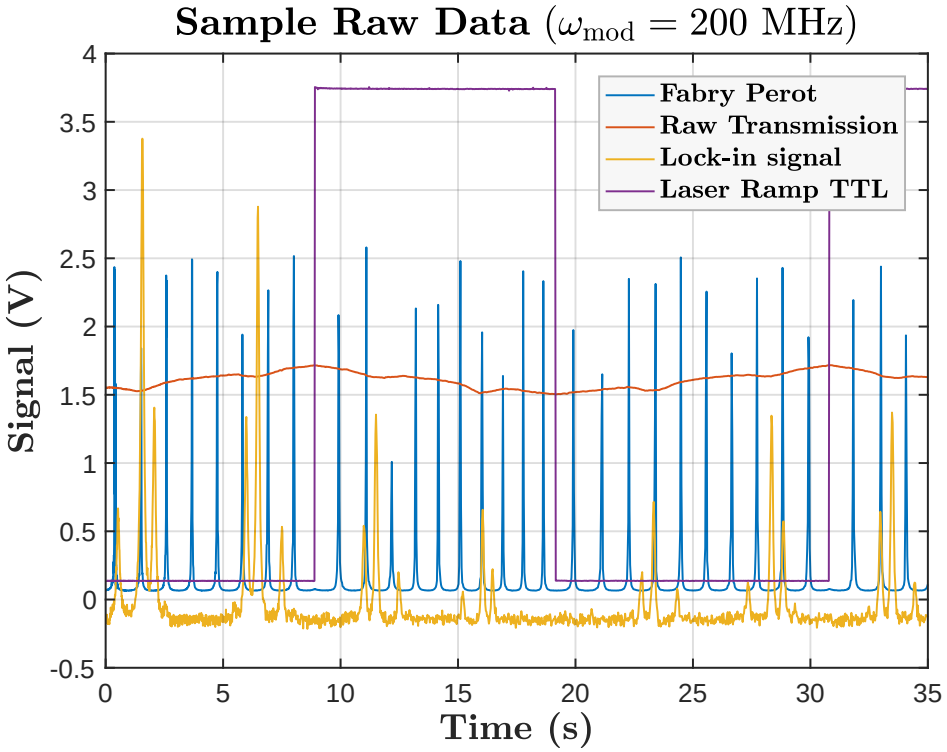


Figure 5.1: Sample raw data of all four channels collected by the LabVIEW program.

# Chapter 6

# Data Analysis

## 6.1 Sample data analysis without EOM sidebands

To get a "zeroth"-order measurement of the isotope shift, we can use our naive method of taking the sum and difference of the co- and counter-peak separations to extract the isotope shifts for both the first- and second-step transitions. As an example, we will walk through the analysis for $^{204}$Pb and $^{208}$Pb.

I collected 1100 s of data on 9 April 2026 at a furnace temperature of approximately 815 °C. The first-step laser was locked at 319.288 790 THz using a wavemeter; this choice made the peak heights roughly equal for both $^{204}$Pb and $^{208}$Pb. Detailed experimental conditions are listed in Appendix A.

The data was sampled at 165 Hz, set by the Nyquist criterion for our lock-in settings. For a lock-in time constant of $\tau_c = 3\,\text{ms}$ and a filter slope of 18 dB per octave, the effective bandwidth is approximately

$$\text{BW} \;\approx\; \frac{1/4}{\tau_c} \;=\; \frac{0.25}{3\,\text{ms}} \;\approx\; 83.3\,\text{Hz}, \tag{6.1}$$

and the maximum sampling rate without correlated points is

$$f_{\max} \;\approx\; 2 \times \text{BW} \;\approx\; 166.7\,\text{Hz}. \tag{6.2}$$

Table 6.1: Sample data collected over 1100 s for $^{204}$Pb and $^{208}$Pb without EOM sidebands, on 9 April 2026.

| | # Upscans | # Downscans | Total |
|---|---|---|---|
| Co-alignment | 16 | 16 | 32 |
| Counter-alignment | 15 | 15 | 30 |
| Total | 31 | 31 | 62 |

### 6.1.1 Preprocessing

I split the raw data into upscans and downscans for co- and counter-alignments using the TTL signal from the function generator that scans the laser, and then flipped the downscans horizontally so that laser frequency increases to the right in every scan. I determined the scan direction by walking the IR laser lockpoint: since the $^{204}$Pb peak should sit at higher frequency than $^{208}$Pb, comparing how the relative peak heights changed for $^{204}$Pb and $^{208}$Pb under different lockpoints fixed the sign convention, and confirmed which scans needed to be flipped.

Each raw data file contains four channels: time, the Fabry–Pérot (FP) etalon signal, the laser transmission signal, and the lock-in spectroscopy signal. Before any fitting, I divide the spectroscopy signal by the simultaneously recorded transmission signal,

$$S(j) \;=\; \frac{I_{\mathrm{spec}}(j)}{I_{\mathrm{trans}}(j)}, \tag{6.3}$$

where $j$ indexes the data point. The transmission channel records the slowly varying laser intensity across the scan, and dividing by it removes the intensity change that would otherwise distort the peak amplitudes and tilt the baseline.

### 6.1.2 Fabry–Pérot frequency calibration

The core problem to solve is that our data is recorded in time, not in frequency. We scan the laser by applying a voltage ramp to a piezoelectric transducer (PZT), but the PZT response is not perfectly linear—the relationship between voltage and frequency has slight curvature—so equal time steps do not correspond to equal frequency steps. Using the sample index as a frequency axis would systematically bias the measured peak separations.

To build a calibrated frequency axis, I use the simultaneously recorded signal from a Fabry–Pérot (FP) cavity. The FP cavity acts as a frequency ruler: it transmits sharp peaks at perfectly regular frequency intervals, each separated by the free spectral range $FSR = 0.999\,62\,\mathrm{GHz}$. These peaks land at uneven spacings in time (because of the PZT nonlinearity), but we know they are exactly one FSR apart in frequency. By fitting the positions of these peaks, we can infer the nonlinear mapping from time to frequency and invert it.

#### The Airy function model

The transmitted intensity through a Fabry–Pérot cavity is described by the Airy function,

$$I_{\mathrm{FP}}(\phi) \;=\; \frac{I_0}{1 + \mathcal{F}\sin^2\phi}, \tag{6.4}$$

where $\phi$ is half the round-trip optical phase inside the cavity and $\mathcal{F} = 4R/(1-R)^2$ is the coefficient of finesse, which controls the sharpness of the peaks ($R$ is the mirror reflectivity).

The peaks occur whenever $\sin\phi = 0$, that is, whenever $\phi = n\pi$ for any integer $n$. Consecutive peaks are separated by $\Delta\phi = \pi$, which corresponds to exactly one free spectral range in optical frequency [11].

The key insight is that $\phi$ is proportional to the laser frequency. If the laser scanned linearly in time, $\phi$ would be a linear function of the sample index. In practice the PZT introduces nonlinearity, so I model $\phi$ as a polynomial. Let $x_j = (j - (N-1)/2)/((N-1)/2) \in [-1, 1]$ be the normalized sample coordinate for a scan of $N$ points. Then

$$\phi(x) \;=\; a_0 + a_1 x + a_2 x^2 + a_3 x^3, \tag{6.5}$$

where $a_1$, $a_2$, $a_3$ capture nonlinearities in the laser scan. In practice a cubic is sufficient for our PZT; higher-order terms do not improve the residuals.

I also allow for a slowly varying intensity baseline across the scan, since the laser power is not perfectly constant, giving the full model

$$I_{\mathrm{FP}}(x) \;=\; C_0 \;+\; \frac{C_1 + C_2\, x}{1 + \mathcal{F}\sin^2[\phi(x)]}, \tag{6.6}$$

with eight free parameters: $\{C_0, C_1, C_2, \mathcal{F}, a_0, a_1, a_2, a_3\}$ [11].

### Fitting procedure

To make this nonlinear model converge well, we need good initial guesses. I use a two-step approach:

1. **Find the FP peaks.** Lightly smooth the FP signal with a Gaussian kernel to suppress high-frequency noise (which can produce spurious peaks), then run a peak-detection algorithm to locate each FP peak in normalized sample coordinates.

2. **Assign phases and pre-fit the polynomial.** Since consecutive FP peaks are separated by exactly $\Delta\phi = \pi$, I label the detected peaks with phase values

   $$\phi_i \;=\; \big(i - \lfloor n/2 \rfloor\big)\,\pi, \tag{6.7}$$

   centered so the middle peak sits near $\phi = 0$ ($n$ is the number of detected peaks). This gives a set of $(x_i, \phi_i)$ pairs—one per peak—which I fit with a cubic polynomial using ordinary least squares. The resulting coefficients seed the full nonlinear fit.

3. **Fit the full Airy model.** Using the polynomial coefficients from the previous step, together with reasonable guesses for the amplitude and finesse parameters, I fit Eq. (6.6) to the entire FP waveform using nonlinear least squares. Fitting the full waveform—not just the peak positions—uses the information in the peak shapes and the valleys between peaks, giving more precise polynomial coefficients.

**Extracting the frequency axis**

The fitted polynomial $\phi(x)$ tells us the optical phase at every sample point. Since the phase advances by $\pi$ for each FSR of optical frequency,

$$f(x_j) \;=\; \frac{\Delta\nu_{\mathrm{FSR}}}{\pi}\,\phi(x_j) \;=\; \frac{\Delta\nu_{\mathrm{FSR}}}{\pi}\big(a_0 + a_1 x_j + a_2 x_j^2 + a_3 x_j^3\big). \tag{6.8}$$

This assigns a calibrated relative frequency to every sample in the scan. The absolute frequency origin is arbitrary (it depends on where the scan happens to start) and cancels exactly when we compute the peak separation, which is the only quantity we care about.

### 6.1.3 Two-Lorentzian fit

Once each scan has its own calibrated frequency axis, I fit the normalized spectroscopy signal $S(f)$ to a sum of two Lorentzians with a common baseline,

$$S(f) \;=\; S_0 \;+\; A_1\,\frac{\Gamma_1/(2\pi)}{(f-f_1)^2 + (\Gamma_1/2)^2} \;+\; A_2\,\frac{\Gamma_2/(2\pi)}{(f-f_2)^2 + (\Gamma_2/2)^2}, \tag{6.9}$$

where $S_0$ is a constant baseline that absorbs any residual phase offset in the lock-in signal, $f_1, f_2$ are the peak centers, $\Gamma_1, \Gamma_2$ the full widths at half maximum, and $A_1, A_2$ the amplitudes. The fit has seven free parameters in total.

Initial guesses for the peak centers and amplitudes are obtained automatically: I take the mean of the first 100 data points as a baseline, and identify the first two regions above some threshold amplitude value as the two peaks. The midpoint of each region gives the initial peak center guess, and the maximum signal within each region (minus the baseline) gives the initial amplitude. These, together with a default FWHM of 0.1 GHz, are enough for the nonlinear least-squares fit of Eq. (6.9) to converge.

From the fitted centers, the peak separation for a given scan is

$$PS^{fit} \;=\; f_2 - f_1, \qquad \sigma_{PS} \;=\; \sqrt{\sigma_{f_1}^2 + \sigma_{f_2}^2}, \tag{6.10}$$

where $\sigma_{f_1}$ and $\sigma_{f_2}$ are the standard errors on the fitted centers, taken to be uncorrelated. See figure 6.1 for a sample up-scan fit. The residuals indicate that the Lorentzian model does not accurately capture the line shape, since the wings fall off more rapidly and the peak is broader at the top, suggesting a Voigt convolution (see figure 2.2). Luckily, this does not shift the fitted center, since both the Lorentzian and the Voigt function are symmetric. However, the residuals themselves are clearly asymmetric—and that is the fingerprint of the Doppler-weighting systematic discussed in Section 6.3. The fitted peak separation from each scan is the input to the isotope-shift extraction described in the next section.

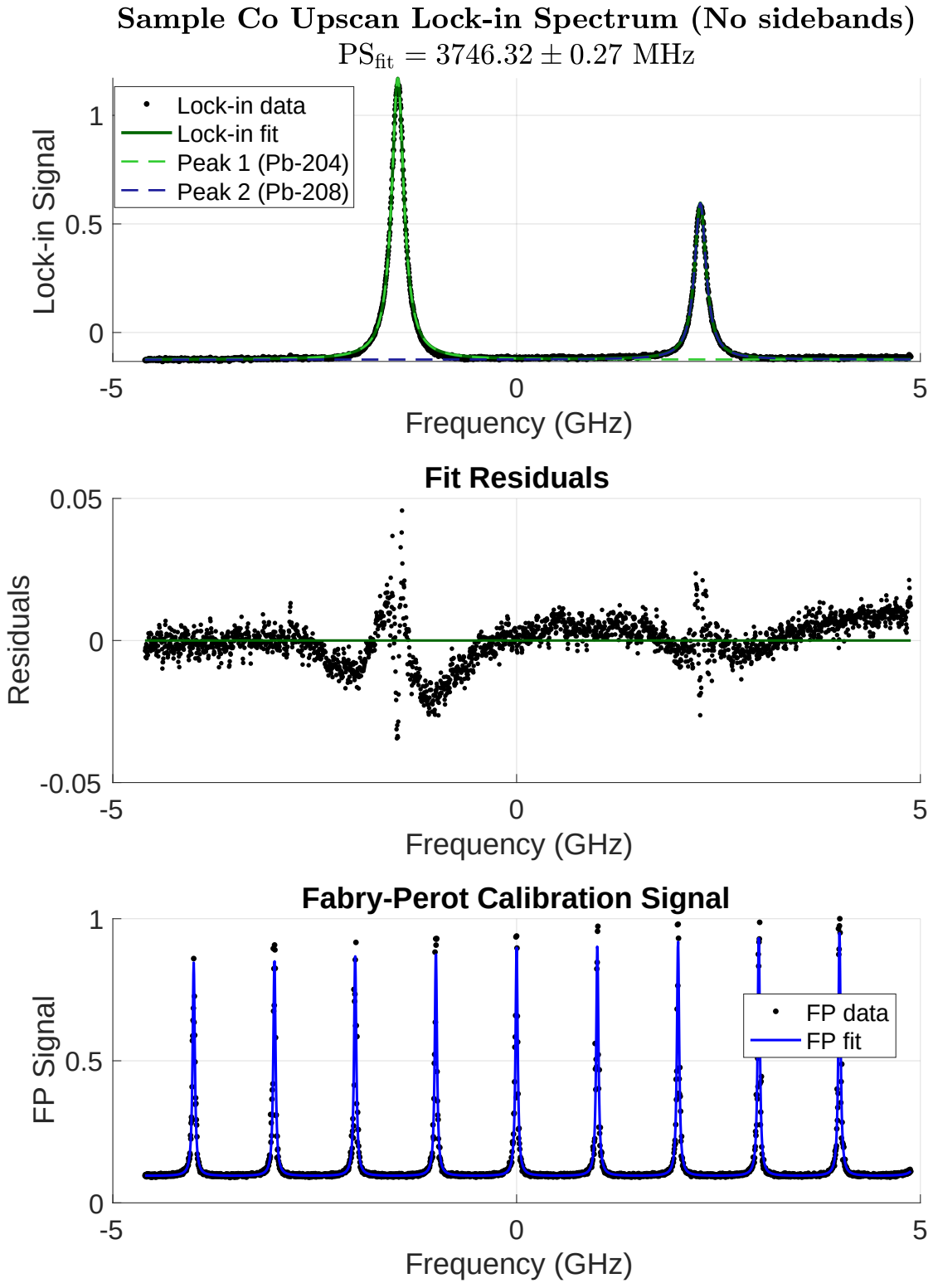


Figure 6.1: Sample up-scan fit without RF modulation.

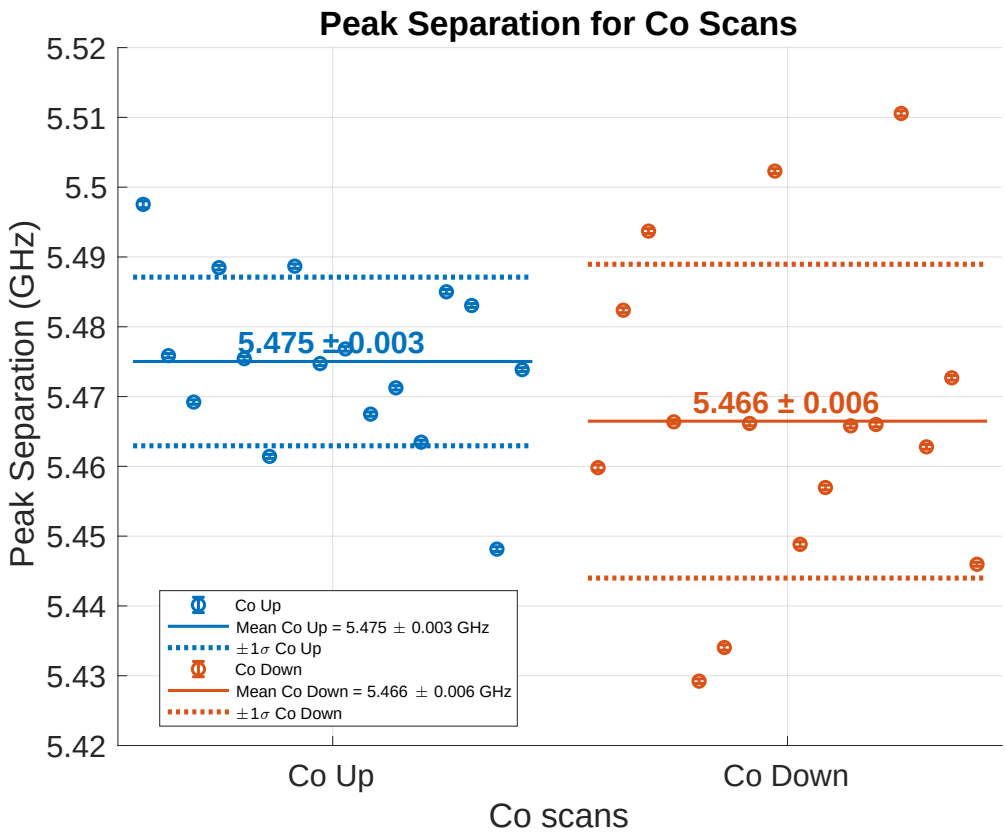


Figure 6.2: Peak separations between the $^{204}$Pb and $^{208}$Pb Lorentzian centers for co-alignment, across all up- and down-scans. Each scan provides a single $PS_{co}$ measurement with its associated fit uncertainty.

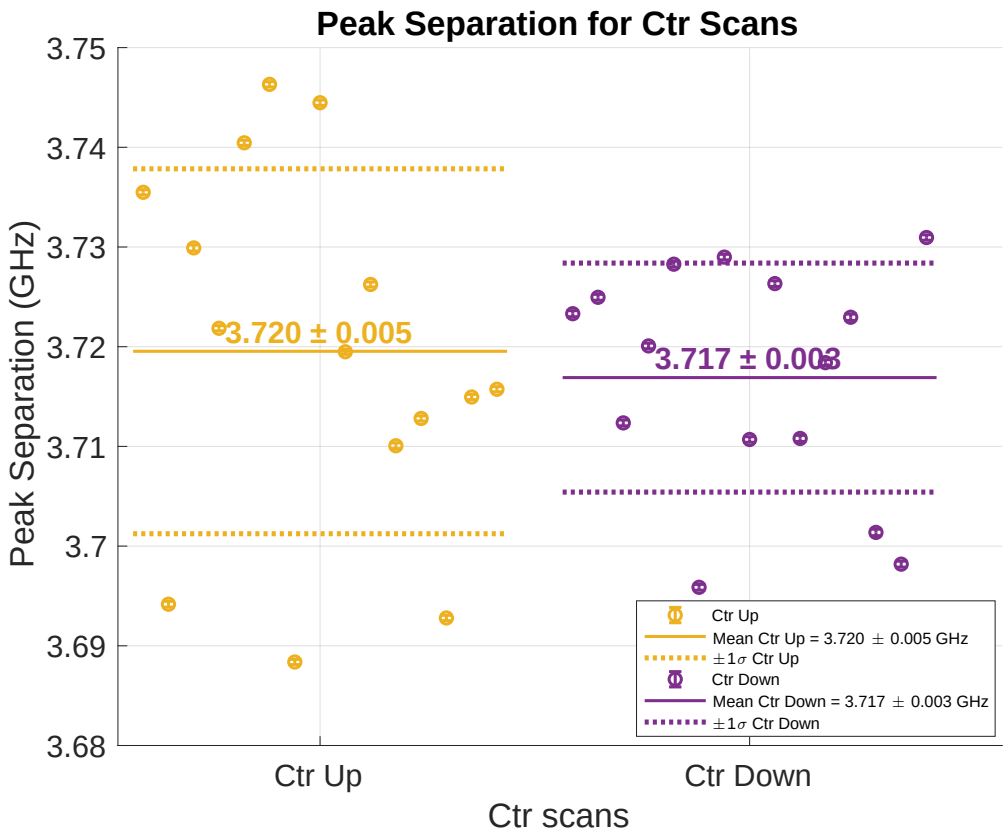


Figure 6.3: Peak separations between the $^{204}$Pb and $^{208}$Pb Lorentzian centers for counter-alignment, across all up- and down-scans.

**Up- vs. down-scan consistency.** Before averaging the peak separations, we check whether sweeping the laser frequency upward versus downward introduces a systematic shift (see figures 6.2 and 6.3). We pair each upscan with its consecutive downscan and perform a paired $t$-test under the null hypothesis that the mean difference between the up- and down-scans is zero. With 16 pairs of co-scans and 15 pairs of counter-scans in the 9 April data, the degrees of freedom are 15 and 14 respectively. The resulting $p$-values are

$$P_{\text{co}} = 0.181, \tag{6.11}$$
$$P_{\text{ctr}} = 0.672. \tag{6.12}$$

This means there is an 18 % and 67 % chance of randomly seeing the observed mean differences of 8.6 MHz and 2.6 MHz for the co- and counter-alignments, respectively, under the null hypothesis. Since $P > 0.05$, we cannot reject the null, which means the up- and down-scans are statistically indistinguishable. We can therefore group all scans within each alignment together and treat them as independent samples of the same peak separation, giving us greater statistical precision in the final measurement of the isotope shifts.

**Combining the scans.** The fit uncertainty per scan is $\sigma_{\text{fit}} \sim 0.3\,\text{MHz}$, much smaller than the scan-to-scan scatter ($\sim 18\,\text{MHz}$ for $PS_{co}$ and $\sim 15\,\text{MHz}$ for $PS_{ctr}$). The dominant uncertainty is therefore not the per-scan fit precision but the run-to-run scatter from drifts in the laser, the FP cavity, and the 939 nm laser lock point. We estimate each peak separation as the mean across all scans, with the standard error as its uncertainty:

$$\overline{PS}_{co} = (5.4708 \pm 0.0032)\ \text{GHz}, \quad N = 32, \tag{6.13}$$

$$\overline{PS}_{ctr} = (3.7182 \pm 0.0028)\ \text{GHz}, \quad N = 30. \tag{6.14}$$

**Extracting the isotope shifts.** Inserting these averages into Eqs. (3.12) and (3.13) and propagating the standard errors,

$$\begin{aligned} IS_{939}^{204/8} &= \frac{k_{939}^{\text{laser}}}{2\,k_{406}^{\text{laser}}}\big(\overline{PS}_{co} - \overline{PS}_{ctr}\big) \\ &= \frac{1}{2}\,\frac{405.895}{938.938}\,\big(5.4708\,\text{GHz} - 3.7182\,\text{GHz}\big) \\ &= \boxed{(378.8 \pm 0.9)\ \text{MHz}}, \end{aligned} \tag{6.15}$$

$$\begin{aligned} IS_{406}^{204/8} &= -\tfrac{1}{2}\big(\overline{PS}_{co} + \overline{PS}_{ctr}\big) \\ &= -\tfrac{1}{2}\big(5.4708\,\text{GHz} + 3.7182\,\text{GHz}\big) \\ &= \boxed{(-4594.5 \pm 2.1)\ \text{MHz}}. \end{aligned} \tag{6.16}$$

The errors follow from

$$\sigma_{IS_{939}} = \frac{k_{939}^{\text{laser}}}{2\,k_{406}^{\text{laser}}}\sqrt{\sigma_{\overline{PS}_{co}}^2 + \sigma_{\overline{PS}_{ctr}}^2}, \qquad \sigma_{IS_{406}} = \tfrac{1}{2}\sqrt{\sigma_{\overline{PS}_{co}}^2 + \sigma_{\overline{PS}_{ctr}}^2}. \tag{6.17}$$

The positive sign of $IS_{939}^{204/8}$ and the negative sign of $IS_{406}^{204/8}$ are consistent with the reversed level ordering described in Section 2.4.

**Discussion.** This zeroth-order measurement already reproduces both isotope shifts at about the 1–2 MHz level. The dominant contribution to the uncertainty is the scan-to-scan scatter in the fitted peak centers, which is in turn driven by drifts in $\omega_{\text{offset}}$ between scans—exactly the systematic that the naive method is supposed to be insensitive to. In practice, the Lorentzian centers are biased by the underlying Doppler–Boltzmann velocity weighting (Section 6.3), and that bias depends on where the laser carrier sits relative to each atomic line. So the naive method does retain a residual sensitivity to $\omega_{\text{offset}}$ through the line shape, even though the kinematic dependence cancels exactly in Eqs. (3.10) and (3.11). The co/counter-crossing method developed in the next section gets rid of this residual bias by extrapolating to the crossing point, where the velocity classes selected by the sidebands are matched between the two isotopes.

## 6.2 Data analysis for the co/counter-crossing method

### 6.2.1 Frequency linearization and fitting

For the co/counter-crossing analysis I apply the same Fabry–Pérot frequency calibration described in Section 6.1.2: the FP signal recorded alongside each scan is fit to the Airy model, and the resulting phase polynomial maps sample index to relative optical frequency. Each calibrated scan is then fit simultaneously to a sum of 14 Lorentzians—a carrier plus six sidebands ($\pm1$, $\pm2$, $\pm3$ orders) for each of $^{204}$Pb and $^{208}$Pb. The full fitting model, initial-guess strategy, and a cross-check on the FP free-spectral-range value are given in Appendix D. As in the no-sideband case, scan-to-scan scatter dominates the per-scan fit uncertainty, so we take the standard error of the mean across scans as the uncertainty on each peak separation. The 160 MHz dataset was discarded due to poor signal-to-noise.

### 6.2.2 Robustness to the polynomial fit order

### 6.2.3 Uncertainty propagation to the intersection point and isotope shifts

The co- and counter-aligned peak separations are each fitted to a linear model in modulation frequency $\omega_{\mathrm{mod}}$:

$$PS_{co} = m_{co}\,\omega_{\mathrm{mod}} + b_{co}, \tag{6.18}$$

$$PS_{ctr} = m_{ctr}\,\omega_{\mathrm{mod}} + b_{ctr}. \tag{6.19}$$

Setting $PS_{co} = PS_{ctr}$ and solving for the intersection gives

$$\omega_{\mathrm{mod}}^{\mathrm{int}} = \frac{b_{ctr} - b_{co}}{m_{co} - m_{ctr}}, \tag{6.20}$$

$$PS^{\mathrm{int}} = m_{co}\,\omega_{\mathrm{mod}}^{\mathrm{int}} + b_{co}. \tag{6.21}$$

For convenience we write $N = b_{ctr} - b_{co}$ and $D = m_{co} - m_{ctr}$, so $\omega_{\mathrm{mod}}^{\mathrm{int}} = N/D$.

Within each fit, slope and intercept are correlated because they are estimated from the same data, and including this within-fit covariance is essential—ignoring it inflates the final uncertainties by roughly an order of magnitude. The full error-propagation derivation and a Monte Carlo verification (which confirms the analytic formulas to within rounding) are given in Appendix E.

**Isotope shifts from the intersection point.** The intersection point $\left(\omega_{\mathrm{mod}}^{\mathrm{int}},\, PS^{\mathrm{int}}\right)$ gives the isotope shifts directly:

$$IS_{939}^{204/8} = 2\,\omega_{\mathrm{mod}}^{\mathrm{int}}, \tag{6.22}$$

$$IS_{406}^{204/8} = -PS^{\mathrm{int}}, \tag{6.23}$$

with uncertainties

$$\sigma(IS_{939}^{204/8}) = 2\,\sigma(\omega_{\mathrm{mod}}^{\mathrm{int}}), \tag{6.24}$$

$$\sigma(IS_{406}^{204/8}) = \sigma(PS^{\mathrm{int}}). \tag{6.25}$$

### 6.2.4 Isotope shift results

Table 6.2 summarizes the analytic and Monte Carlo uncertainties for the intersection point and the extracted isotope shifts. The two methods agree to within rounding, confirming the analytic error propagation.

| Quantity | Analytic (MHz) | Monte Carlo (MHz) |
|---|---|---|
| $\omega_{\mathrm{mod}}^{\mathrm{int}}$ | $190.59 \pm 0.30$ | $190.59 \pm 0.36$ |
| $PS^{\mathrm{int}}$ | $4589.6 \pm 1.4$ | $4589.7 \pm 1.6$ |
| $IS_{939}^{204/8}$ | $381.2 \pm 0.6$ | $381.2 \pm 0.7$ |
| $IS_{406}^{204/8}$ | $-4589.6 \pm 1.4$ | $-4589.7 \pm 1.6$ |

Table 6.2: Intersection-point coordinates and isotope shift values with uncertainties from analytic error propagation and Monte Carlo simulation.

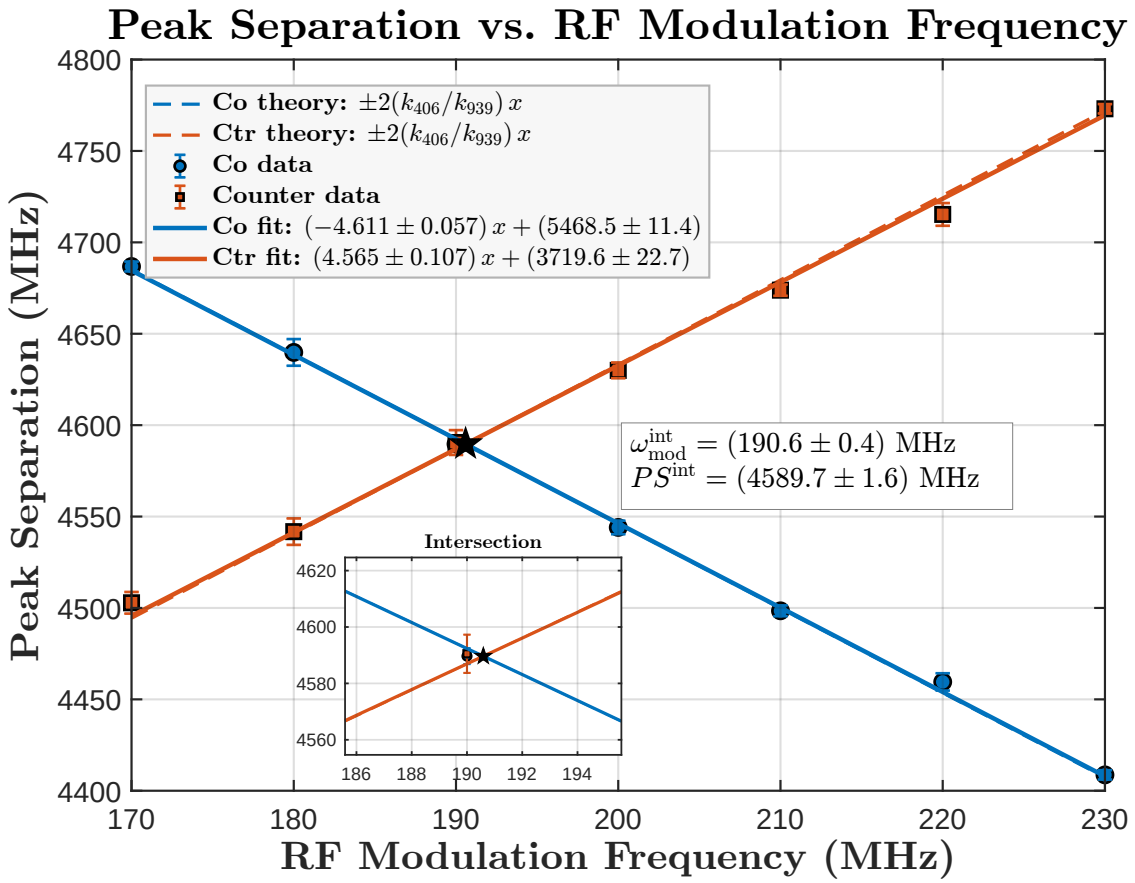


Figure 6.4: Peak separations vs. modulation frequency for $^{204}$Pb and $^{208}$Pb.

The co/counter-crossing method reduces the isotope-shift uncertainties by about 20 % compared with the naive sum-and-difference approach of Section 6.1.

## 6.3 Systematic effects

Note that the slopes of the co and counter plots should be given by twice the wavevector ratio, $\pm 2\,k_{406}/k_{939} \approx \pm 4.626$. The co and counter fits in our 9 April $^{204/8}$Pb data both give slopes that are smaller than the theoretical values, though they are both within the error bars in this case ($0.26\sigma$ and $0.72\sigma$ away respectively). Whether or not this is truly a systematic becomes clearer if we probe a larger range of modulation frequencies, since the deviation from the theoretical line grows the farther we are from the intersection point. For instance, before we collected the narrow-range data above, we took preliminary data on $^{207}$Pb and $^{208}$Pb over a much larger range of modulation frequencies (500 MHz versus the 70 MHz window around the intersection used for the 9 April data) and with about five times as many data points. See figure 6.5 for the resulting peak separation vs. RF modulation for $^{207}$Pb and $^{208}$Pb. In this case the slope uncertainties were much smaller, and both alignments sit

about 2 % below the theoretical value at $4.3\sigma$ and $9.5\sigma$ away for co and counter respectively (table 6.3). This strongly suggests that, although the percent-level error in the slopes of the 204–208 data is within the noise, the same systematic is present there too—just hidden by the larger uncertainties.

In the rest of this section we trace this discrepancy to Doppler-velocity weighting of the line shape and show why it leaves the crossing point untouched, then list the other candidates we considered along the way. A handful of additional smaller corrections are cataloged in Appendix C.

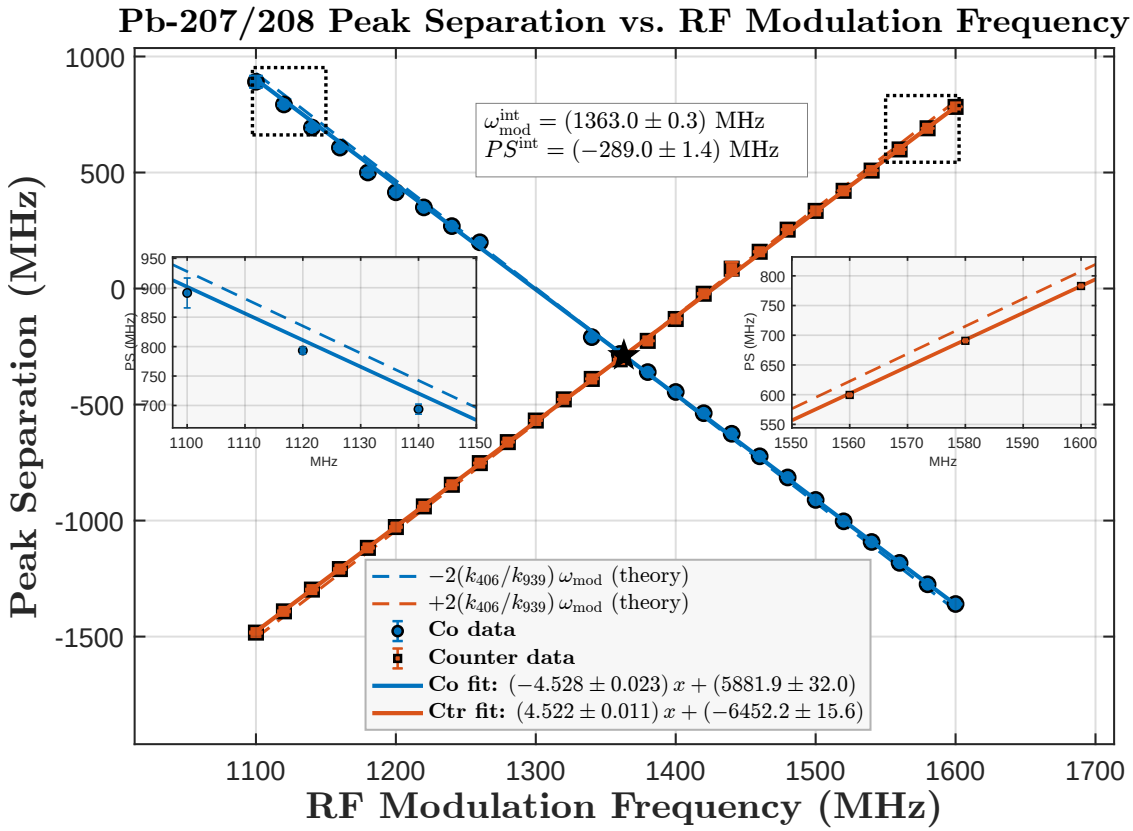


Figure 6.5: Peak separations vs. modulation frequency for $^{207}$Pb and $^{208}$Pb. The wide modulation-frequency range resolves the 2 % slope systematic.

The same systematic also shows up as the asymmetric residuals in the no-sideband fits of figure 6.1. This systematic error puzzled us for a few months, but we were eventually able to confirm that the slope shift was at least in part due to Doppler weighting of the Lorentzian curves—and, crucially, that it does not affect the location of the intersection point.

Table 6.3: Measured slopes ($\mathrm{d}PS/\mathrm{d}\omega_{\mathrm{mod}}$) compared with the theoretical $2\,k_{406}/k_{939} \approx 4.626$.

| **Dataset** | **Alignment** | **Measured Slope** | **Uncertainty** | **Theory Slope** | **% Diff** | **Agreement ($\sigma$)** |
|---|---|---|---|---|---|---|
| 204–208 | CO | −4.611 | 0.057 | −4.626 | 0.32% | $0.26\sigma$ ✓ |
| 204–208 | CTR | +4.565 | 0.085 | +4.626 | 1.32% | $0.72\sigma$ ✓ |
| 207–208 | CO | −4.528 | 0.023 | −4.626 | 2.12% | $4.3\sigma$ ✗ |
| 207–208 | CTR | +4.522 | 0.011 | +4.626 | 2.25% | $9.5\sigma$ ✗ |

### 6.3.1 Doppler velocity weighting

The systematic error in the slope is a result of the Boltzmann distribution of the Pb atoms. Because the velocity distribution has finite width, the number of atoms per velocity class changes across the peak. When the pump laser is parked off-resonance, it excites an asymmetric velocity distribution of atoms to the intermediate excited state. Since the observed second-step signal is proportional to the number of atoms, one side of the peak is disproportionately amplified, resulting in a skewed Lorentzian. If we fit the result to a regular Lorentzian, the center shifts in the direction of the center of the Boltzmann distribution—and that's where the slope discrepancy comes from.

According to our analysis of the Doppler weighting effect, the slope is not only going to be systematically lower than the theoretical value, but it is also expected to vary with the location of the carrier lock point and the modulation frequency. We tested both of these predictions.

**Single-isotope lock-point experiment.** Firstly, to test our Doppler weighting hypothesis, we collected data on a single isotope ($^{208}$Pb) with the modulation frequency fixed at $\omega_{\mathrm{mod}} = 300\,\mathrm{MHz}$ and the carrier walked through a range of different lock points. At each lock point we extracted the separation between the carrier and each of the +1 and -1 sidebands, and divided it by 300 MHz to recover frequency ratio $k_{406}/k_{939}$. We plotted it against the lock point; see figures 6.6 and 6.7 for the result. We see that the recovered frequency ratio is always lower than the expected value, since the carrier and sideband peaks are sucked in together toward the center of the Gaussian after weighting, with +1 and -1 sideband separations varying according to the location of the carrier with respect to the Gaussian. The sideband separations are equal only when the carrier is at the Gaussian center, and both sidebands are pulled in equally.

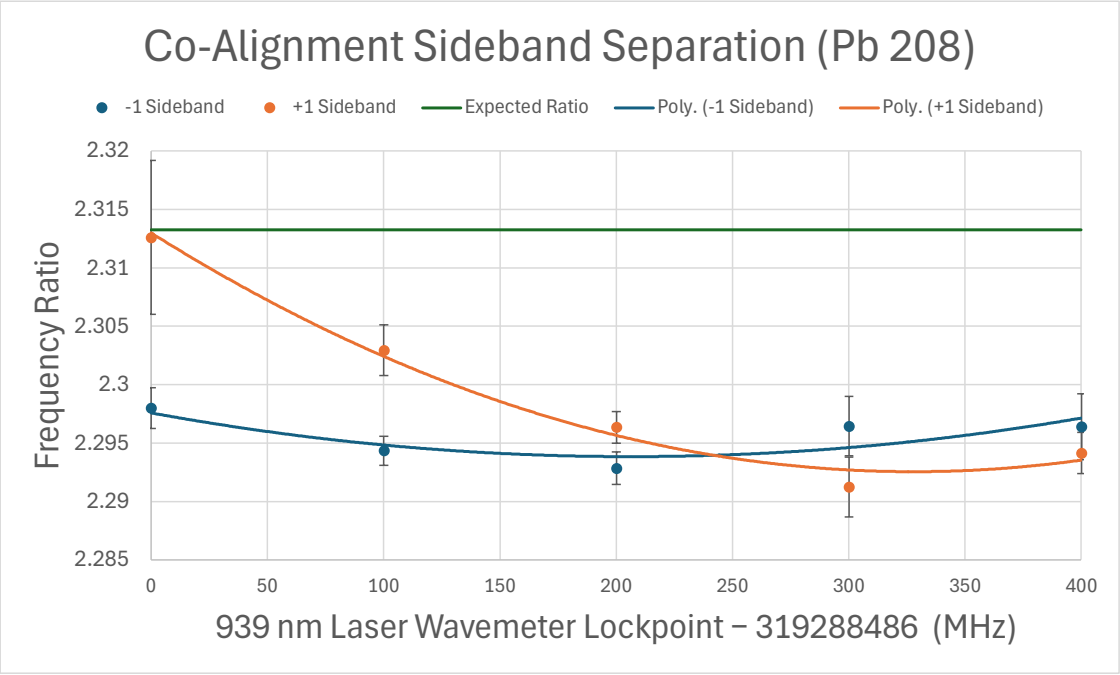


Figure 6.6: Sideband separation for different first-step laser lock points, co-aligned beams, single isotope ($^{208}$Pb).

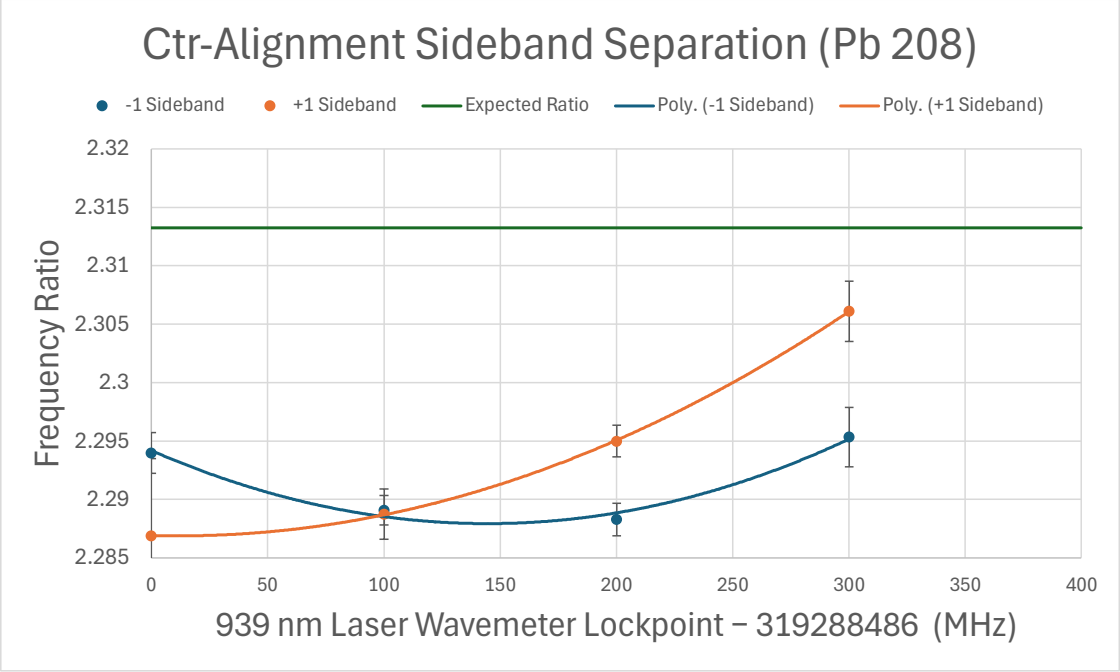


Figure 6.7: Sideband separation for different first-step laser lock points, counter-aligned beams, single isotope ($^{208}$Pb).

**Simulation.** This agrees with our simplified simulation, where we take the product of a sum of three Lorentzians (carrier plus the two first-order sidebands) with a Gaussian (the 1D velocity distribution of the atoms) and fit the result back with another sum of three Lorentzians—exactly the same way we process the raw data—and look at how the sideband separations change. We verify the same qualitative trend in the simulated Doppler-weighting for co-alignment shown in figure 6.8 as in the experimental data above; the counter-aligned version is just the horizontal flip of this. Note that we have zoomed in on the y-axis for all the plots, and that the sideband separations are always systematically lower than the expected frequency ratio because the peaks are drawn in towards the Gaussian center. The simulation plot was restricted to −110 to +110 MHz because the Lorentzian amplitudes were too small to reliably fit when far away from the Gaussian center.

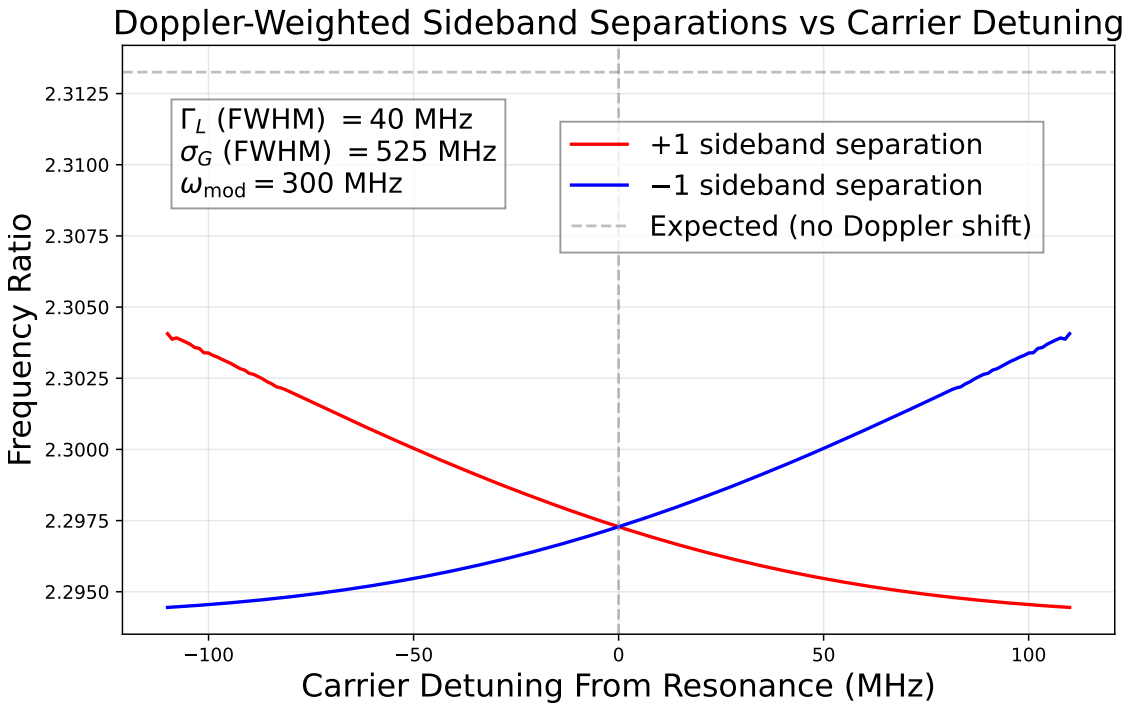


Figure 6.8: Simulated sideband separation for different carrier detunings with co-aligned beams and a single isotope. The counter-aligned case is the horizontal mirror of this plot.

### 6.3.2 Why the crossing point is immune

To figure out how this Doppler weighting effect translates to the two-isotope peak separation, we have to think about where the first- and second-order sidebands sit with respect to the resonances of *both* isotopes, not just one. If a sideband crosses a resonance, the direction of the systematic shift flips on the other side. The frequency at which either sideband crosses an isotope resonance depends on $\omega_{offset}$, which we don't actually know.

There is a region around the intersection point of size $\sim 2\,\omega_{mod}$ within which the systematic deviation from the theoretical peak separations vanishes, because both relevant sidebands sit on the same side of their respective isotope lines, so the Doppler weighting common to both drops out. (Strictly speaking, a small $\sim 33\,\text{kHz}$ residual survives because the two isotopes have slightly different Boltzmann widths; we discuss this in Appendix C.) Outside this region, the two sidebands are on opposite sides of their respective isotope lines, and the Doppler-weighting errors add. Looking at the first-step transition: if both the $^{208}$-sideband and the $^{204}$-sideband are on the inside of their isotope lines, the peaks are pulled apart and the peak separation comes out larger than expected, whereas if both are on the outside, they are drawn together and the separation comes out smaller. When one is inside and the other is outside, however, they shift in the same direction, which leads to almost no net error in the peak separation.

To maximize the systematic-free region, it might be advantageous to push $\omega_{mod}$ as large as possible, so that the sidebands are not both inside or outside for a larger range of modulation frequencies. In practice there are many fewer atoms far from the natural resonances, so the signal-to-noise of the peaks would diminish greatly; there is a balance to be found.

**Is $PS$ vs. $\omega_{\text{mod}}$ really linear?** Although the data looks perfectly linear, our simulation of the systematic shows that the relationship between peak separation and modulation frequency is actually nonlinear due to the Doppler weighting. Looking at the simulated slope vs. frequency, however, the slope only varies by about one part in $10^6$ across the modulation frequencies we probe, with the maximum slope sitting right at the intersection of the co and counter lines. We can therefore make a first-order Taylor approximation and treat the slope as constant within $\pm 40\,\text{MHz}$ of the intersection, which justifies using a straight line to fit the data. For the 204–208 data, I tested higher-order polynomial fits alongside the linear one and there was no noticeable improvement in the residuals. Since the systematic produces a complicated $PS$ vs. $\omega_{mod}$ line shape that we do not yet fully understand, we find it hard to justify a more complicated fitting function when the linear fit works so well to describe our data.

### 6.3.3 Other systematic effects considered

Before settling on Doppler weighting as the explanation, we briefly considered a few other systematics, including three-level coupling effects, changes in the refractive index near the atomic resonance, and drifts in alignment and beam overlap. At first glance, since the second-step E1 transition is orders of magnitude stronger than the first-step E2 transition, we think three-level coupling is probably not a strong systematic here. Next, the atomic density in our vapor cell is so low that we don't expect to see refractive-index effects. Lastly, the beam angles that would be required to produce the systematic we observe seem unrealistic in our apparatus, since the millimeter-sized beams stay overlapped over a couple of meters. That said, all three of these effects deserve a more careful look.

# Chapter 7

# Next Steps

## 7.1 Calibrate the Fabry Perot Cavity

This is a necessary step to reduce systematic error since all our fits rely on the frequency axis linearization that depends on the free spectral range of the Fabry Perot cavity. Our cavity has not been calibrated in many months, so it must be done before any real data can be taken. This just involves using the free-space EOM to add sidebands of known frequency to the 406 nm laser with which we can accurately determine the frequency spacing between the FP fringes.

## 7.2 Make isotope shift measurements!

Carry out the co and counter crossing experimental method for all the pairs of isotopes and the other set of transitions (368 nm and 1279 nm). We don't have to use every single combination as long as we perform all measurements with reference to one isotope; the rest can be inferred. In our experiment we choose to pair $^{208}$Pb with all the other isotopes, as it is the one we care about the most. Additionally, we also make sure to get all the direct measurements with $^{206}$Pb in case there are systematic errors with the $^{208}$Pb cell.

# Appendix A

# Experimental conditions

| **Parameter** | **Value** |
|---|---|
| Cells | $^{204}$Pb and $^{208}$Pb (separate cells) |
| Furnace temperature | 825 °C (start), 806 °C (end) |
| 406 nm laser scan rate | 15 s per scan |
| 939 nm laser lock point | 319.288 790 THz |
| Lock-in time constant | 3 ms |
| Lock-in sensitivity | 10 $\mathrm{mV_{rms}}$ |
| Lock-in filter | 18 dB/oct |
| EOM sidebands | None |
| AOM modulation | 110 MHz, +8.0 dBm |
| 406 nm laser power | 3.0 mW to 3.6 mW |
| 939 nm power (CO entrance) | 2.68 mW |
| 939 nm power (CTR entrance) | 2.22 mW |
| LabVIEW sampling rate | 165 Hz |
| Furnace condition | Evacuated prior to experiment |
| 406 laser temperature | 22.300 °C |
| 406 laser current | ∼28.450 mA |

Table A.1: Experimental conditions for data taken on 9 April 2026.

# Appendix B

# Tips on Optimizing the Signal, and Good Practices in Building Optics

## B.1 Tips to Future Students on Optimizing the signal, and Good Practices in building optics

Ensure that the beam is focused at the center of the furnace. This can be done by placing a mirror at the entrance of the furnace to reflect the beam to the side, and following it with a card to see how it changes with distance. Configure lenses so that the beam is narrow at the distance where you expect it to be at the center of the furnace, where the vapor cells are. Heat the furnace temperature sufficiently high to increase atomic density. Note non-linearity in the Pb vapor pressure which dramatically increases above 750 °C (Charles Yang Appendix C). Tighten down all screws firmly. There have been many instances where I have accidentally bumped a mirror, and wasted a lot of time realigning. This includes the screws to mount the optic to the table, the post to the post holder, and the post to the mirror. Walking the beam to optimize the signal. Once you have the signal roughly optimized, choose two mirrors, ideally far away from each other, and start with, say the horizontal knobs. Turn knob A just a little, noting the direction, then optimize knob B, and remember the signal amplitude. Turn knob A either in the same or opposite direction depending on whether the signal has increased or decreased, and optimize B again. Keep repeating until you have explored the entire parameter space to find the globally optimized position. Fiber coupling. It is essential to tighten down all screws in the post mounts and cage as coupling efficiency is extremely sensitive to alignment. Use a fiber pen to send light in the opposite direction and make it overlap with the incoming beam. The degrees of freedom include the lens distance and the horizontal and vertical knobs of two mirrors. If expected efficiency is not achieved, try cleaning the fiber tip as dirt may reduce the coupling efficiency. It is good practice to use the screw holes of the optics table as a reference when designing the beam path so that the beam travels along the grid, and can reflect off of mirrors at 45 degree angle of incidence for optimal efficiency.

# Appendix C

# Smaller systematic corrections

This appendix collects a handful of smaller systematic effects that bias the individual peak-separation measurements but—like the Doppler-velocity weighting discussed in Section 6.3—either cancel at the crossing point or are small enough not to affect the extracted isotope shifts at our current level of precision.

## C.1 Change in beam pointing of the 406 nm laser across the scan

The design of the 406 nm laser is such that the beam pointing changes across the scan. The piezo crystal expands and contracts with the voltage ramp applied across it, which nudges the angle of the metal arm and changes both the external-cavity length and the diffraction-grating angle. Although there is a mirror mounted on the same metal arm to minimize the resulting change in beam pointing, it is not perfect, and any small change in pointing only grows larger downstream. Given that the pump and probe beam diameters are only a few millimeters, even a slight variation in angle could have a noticeable effect on the beam overlap in the furnace across the scan.

## C.2 Momentum kick from absorbing a pump photon

When a Pb atom in the ground state absorbs a 939 nm pump photon, it picks up a small momentum kick in the direction the photon was travelling. The resulting velocity change is

$$v_{\text{kick}} \;=\; \frac{h}{M\,\lambda_{939}} \;\approx\; 2.1\,\text{mm}\,\text{s}^{-1}, \tag{C.1}$$

where $M \approx 204\,m_p$ is the approximate atomic mass. Now that the atom is moving at $v_{\text{kick}}$, the 406 nm probe it sees is Doppler-shifted by

$$\Delta\nu_{406} \;\approx\; \nu_{406}\,\frac{v_{\text{kick}}}{c} \;\approx\; 5\,\text{kHz}, \tag{C.2}$$

with the sign depending on whether the pump and probe beams co- or counter-propagate.

The two isotopes do not get exactly the same kick: $^{204}$Pb is slightly lighter than $^{208}$Pb, and the two also have slightly different first-step transition frequencies, so the pump photon energies (and the resulting velocity kicks) come out a little different. After running through the Doppler formula for each isotope separately, the per-direction recoil shift differs between $^{204}$Pb and $^{208}$Pb by about 98 Hz. And because the co- and counter-aligned kicks point in opposite directions, this systematic flips sign between the two alignments.

This is exactly the structure that makes the crossing method robust. The *second*-step isotope shift, which is proportional to $PS_{co} + PS_{ctr}$, has the co and ctr contributions cancel out, so the recoil bias is essentially zero. The *first*-step shift, which is proportional to $PS_{co} - PS_{ctr}$, has them add up instead, and we end up with a systematic *decrease* of about 42 Hz in the measured first-step isotope shift. This is well below the noise in our measurement (which sits at the MHz level), so we can safely ignore it.

## C.3 Slightly different Doppler widths of the two isotopes

At the crossing point $\omega_{\mathrm{mod}} = IS_{939}^{204/8}/2$, the relevant co-aligned sidebands address each isotope at the same detuning $\delta = \omega_{\mathrm{offset}}$ from its respective atomic line, and therefore at the same lab-frame velocity. The Boltzmann weighting on each peak would then be identical—and the biases from Section 6.3.1 would cancel exactly—if the two isotopes had the same 1D velocity distribution.

They do not. Because $m_{204}$ and $m_{208}$ differ by about 2 %, their Doppler widths $\sigma_i = k_{406}\sqrt{k_B T/m_i}$ differ by about 1 %:

$$\frac{\Delta\sigma_v}{\sigma_v} \;=\; \frac{1}{2}\,\frac{\Delta M}{M} \;\approx\; 0.96\,\%. \tag{C.3}$$

The two peaks therefore experience slightly different Boltzmann weighting, and the resulting differential bias does not cancel in $PS_{\mathrm{co}}$ or $PS_{\mathrm{ctr}}$.

From Eq. (2.15), the peak shift for each isotope is

$$u^{(i)} \approx -\frac{\gamma_L^2\,\omega_{\mathrm{offset}}}{2\sigma_i^2}, \tag{C.4}$$

where $\sigma_i^2 = k_{406}^2\,k_B T/m_i$. The ratio of squared Doppler widths is set by the mass ratio:

$$\frac{\sigma_{208}^2}{\sigma_{204}^2} = \frac{m_{204}}{m_{208}} = \frac{204}{208} \approx 0.981. \tag{C.5}$$

The difference in peak shifts between the two isotopes is

$$\begin{aligned} u^{(208)} - u^{(204)} &= -\frac{\gamma_L^2\,\omega_{\text{offset}}}{2}\left[\frac{1}{\sigma_{208}^2} - \frac{1}{\sigma_{204}^2}\right] \\ &= u^{(208)}\left[1 - \frac{m_{204}}{m_{208}}\right] \\ &\approx 0.019 \times u^{(208)}. \end{aligned} \tag{C.6}$$

The systematic that survives in the peak separation is reduced by a factor of about 50 relative to the single-peak bias.

**Worst-case residual.** Combining the maximum single-peak bias from Eq. (2.17) with the 2 % mass-difference factor:

$$\left|u^{(208)} - u^{(204)}\right|_{\max} \approx 0.02 \times \frac{\gamma_L^2}{2\sigma} \approx 33\,\text{kHz}. \tag{C.7}$$

This is well below both our statistical uncertainty and the resolution of the current measurement. In practice, the first-step lock is set close to the midpoint between the two isotopes ($|\omega_{\text{offset}}| \ll \sigma$), so the actual systematic is even smaller. Note also that this correction is further suppressed for isotope pairs that sit closer in mass.

## C.4 Misalignment of the co and counter beams

If the co- and counter-propagating beams are not exactly anti-parallel through the vapor, the velocity classes selected by the two alignments differ by a $\cos\theta$ factor, where $\theta$ is the small angle between them. This propagates into a residual shift on the peak separation that does not cancel at the crossing point.

# Appendix D

# 14-Lorentzian fitting procedure

## D.1 14-Lorentzian fitting model

The co/counter-crossing analysis requires fitting scans that contain many sidebands. Both $^{204}$Pb and $^{208}$Pb are fit simultaneously to a sum of 14 Lorentzians—carrier plus three pairs of sidebands—plus a constant baseline,

$$\mathcal{L}(x) = b_0 + \sum_{j\in\{204,208\}} \sum_{n=-3}^{+3} A_j(n)\, \frac{\Gamma_j/(2\pi)}{\left[x - (c_j + n\,\Delta\nu)\right]^2 + (\Gamma_j/2)^2}. \tag{D.1}$$

The free parameters are: the baseline $b_0$; the $^{204}$Pb and $^{208}$Pb carrier positions $c_{204}$ and $c_{208}$ (or equivalently $c_{204}$ and the carrier separation $\Delta c = c_{208} - c_{204}$); the widths $\Gamma_{204}$ and $\Gamma_{208}$; the sideband amplitudes $A_j(n)$ ($7 \times 2 = 14$ in total); and the sideband spacing $\Delta\nu$, tied to the RF modulation frequency. The sideband spacing $\Delta\nu$ is recovered from the fitted value and converted back to an RF modulation frequency via the known wavelength scaling factor. where $PS_{\mathrm{co}}^{\mathrm{phys}}$ and $PS_{\mathrm{ctr}}^{\mathrm{phys}}$ are the predictions from Eqs. (3.22) and (3.23), evaluated with ballpark isotope shifts $IS_{939}^{\mathrm{guess}} = 374.8\,\mathrm{MHz}$ and $IS_{406}^{\mathrm{guess}} = -4592.2\,\mathrm{MHz}$.

Within each group of seven peaks, the Lorentzians share a common spacing, and I set the initial guess for that spacing to the ratio of laser frequencies times the RF modulation frequency. I deliberately did not hard-code the Lorentzian spacings, because the free spectral range of the Fabry–Pérot peaks was already fixed at $FSR = 0.999\,62\,\mathrm{GHz}$ , and I did not want to over-constrain the model. See figures D.2 and D.1 for sample up-scan fits at $\omega_{\mathrm{mod}} = 200\,\mathrm{MHz}$ and $\omega_{\mathrm{mod}} = 220\,\mathrm{MHz}$ respectively. The modulation depth changes with frequency because the amplifier gain is frequency-dependent: in the 200 MHz data essentially all power goes into the sidebands and none into the carrier, while in the 220 MHz data the carrier is clearly present. The frequency difference between the dotted lines—which mark the relevant $+1$ and $-1$ sidebands—is the peak separation. The residuals of the lock-in signal fits are homoscedastic, indicating the model captures the data well.

Table D.1: Initial guesses for the 14-Lorentzian fit parameters. All parameters are unconstrained (free).

| **Param.** | **Physical meaning** | **Initial guess** |
|---|---|---|
| $b_0$ | Baseline offset | Average of first 100 data points |
| $c_{204}$ | $^{204}$Pb carrier (GHz) | Hard-coded based on visual inspection |
| $\Gamma_{204}$ | $^{204}$Pb FWHM (GHz) | Median of detected peak widths; $\geq 0.05$ GHz |
| $A_{204}^{(n)}$ | $^{204}$Pb amplitudes ($n = -3, \ldots, +3$) | Mean height of $^{204}$Pb region; $\geq 0.01$ |
| $\Gamma_{208}$ | $^{208}$Pb FWHM (GHz) | Same as $\Gamma_{204}$ |
| $A_{208}^{(n)}$ | $^{208}$Pb amplitudes ($n = -3, \ldots, +3$) | Mean height of $^{208}$Pb region; $\geq 0.01$ |
| $\Delta\nu$ | Sideband spacing (GHz) | $\omega_{\mathrm{mod}} \times k_{939}/k_{406}$ |
| $\Delta c$ | Carrier separation (GHz) | $(PS_{\mathrm{co}}^{\mathrm{phys}} + 2\Delta\nu)$ or $(PS_{\mathrm{ctr}}^{\mathrm{phys}} - 2\Delta\nu)$ |

## D.2 FP free-spectral-range cross-check

There is possibly a systematic error from the FSR value used to calibrate the frequency axis, since the FP cavity has not been calibrated in months. To probe for it, I chose the 220 MHz batch of scans and reverse-engineered the RF modulation frequency from the Lorentzian spacing that the fit returned, by dividing the fitted spacing by the laser frequency ratio. The result was that the reverse-engineered frequencies came in about 0.28 % below the nominal 220 MHz, roughly 8 standard errors away (figure D.3). This strongly suggests the FSR value used in the calibration is slightly too large, since we trust the 220 MHz from the RF synthesizer to be exact. For the purposes of this thesis—a proof-of-concept demonstration of the co/counter-crossing method—this systematic is small enough not to concern us.

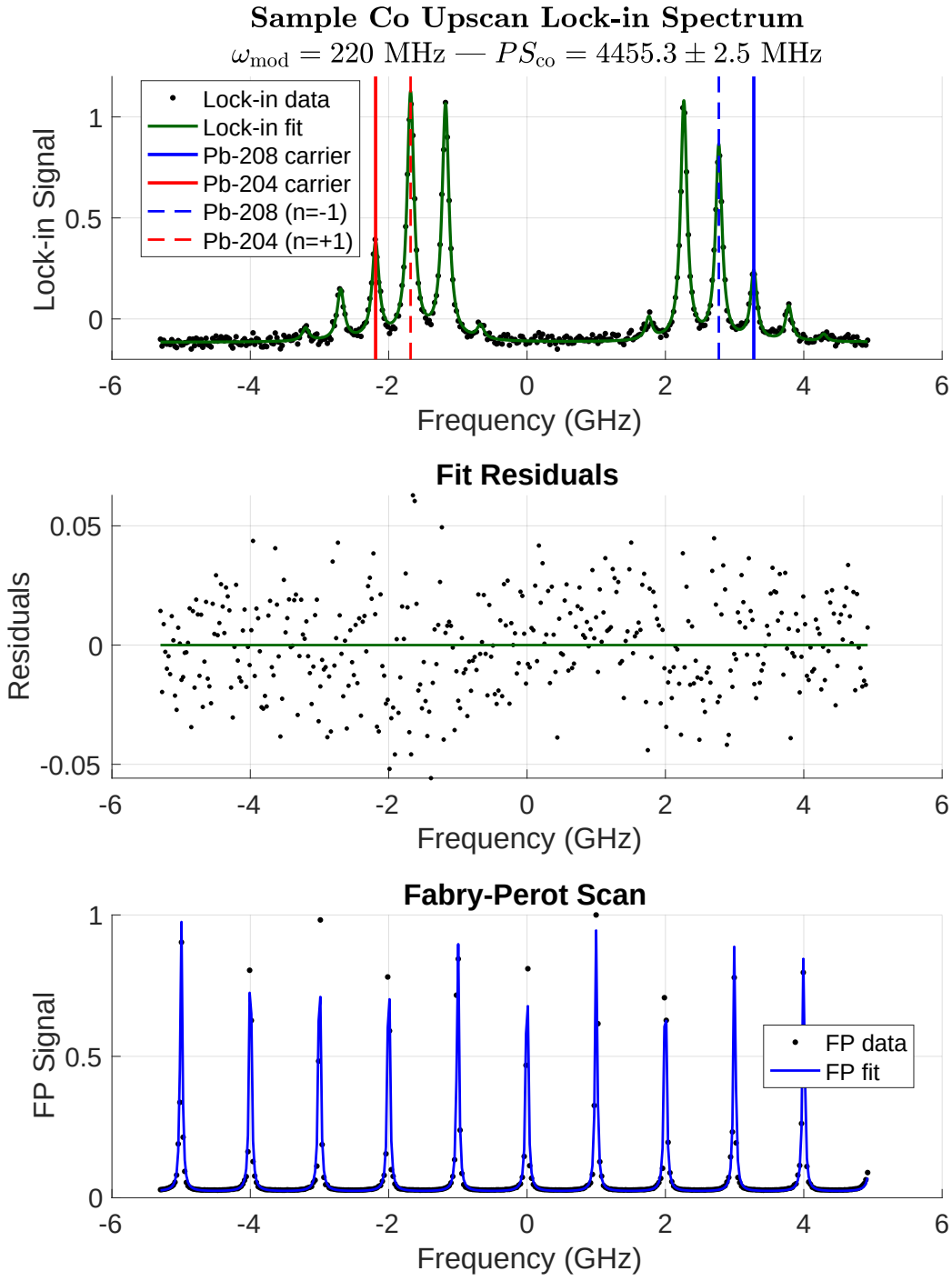


Figure D.1: Sample fitted up-scan for co-alignment at $\omega_{\text{mod}} = 220\,\text{MHz}$.

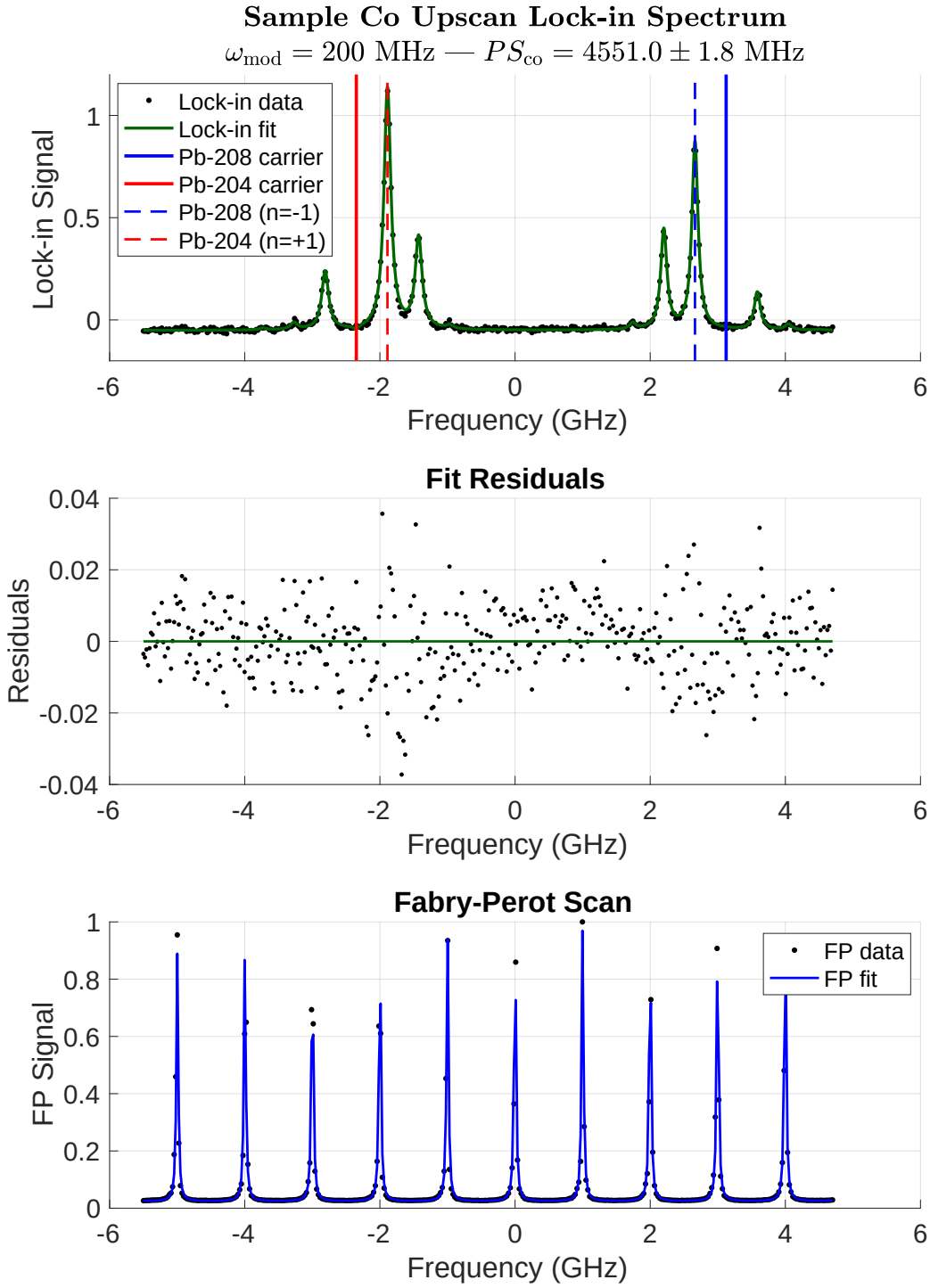


Figure D.2: Sample fitted up-scan for co-alignment at $\omega_{\mathrm{mod}} = 200\,\mathrm{MHz}$. The modulation depth puts essentially all power into the sidebands, suppressing the carrier.

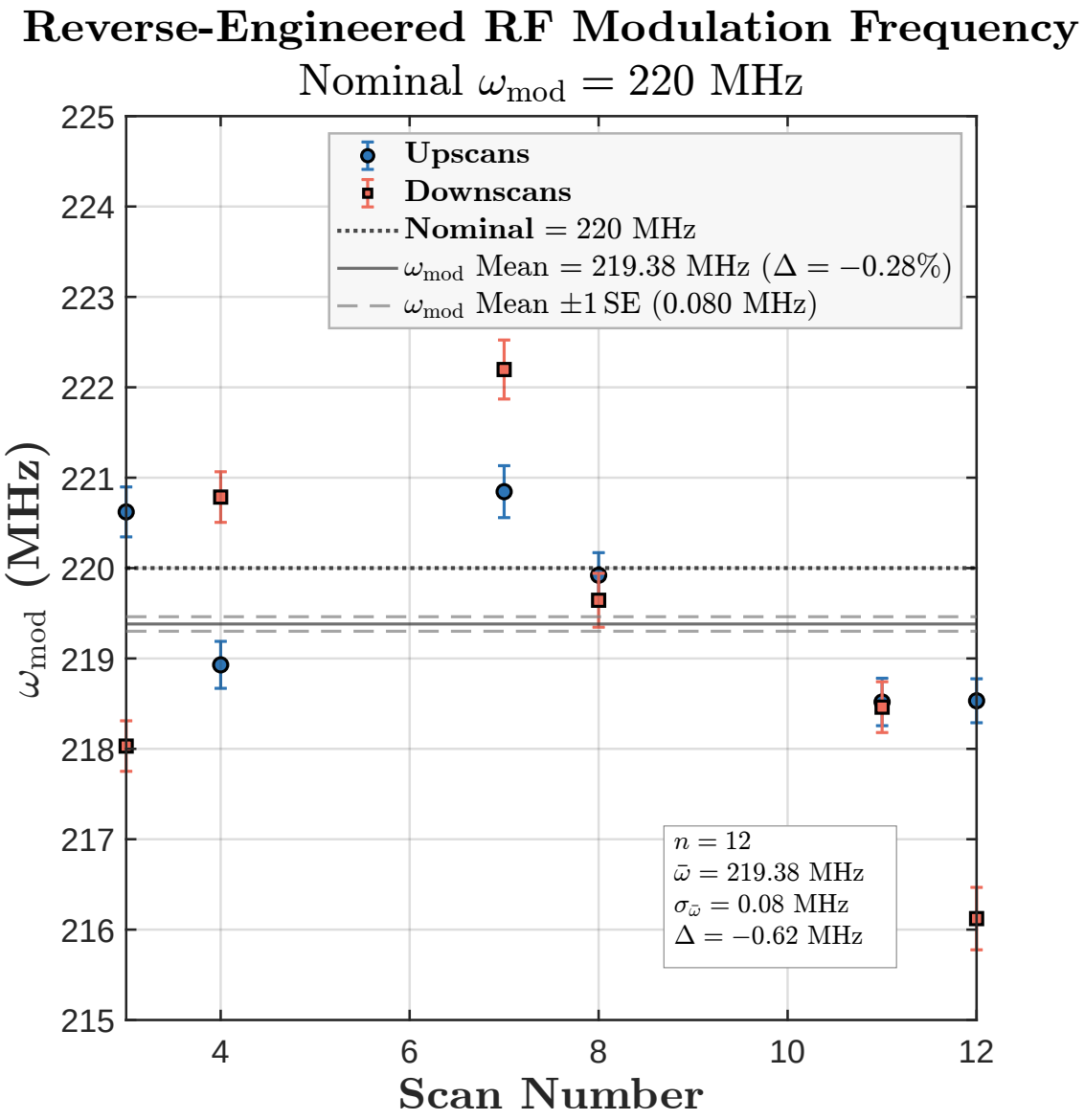


Figure D.3: Reverse-engineered modulation frequency for the $\omega_{\text{mod}} = 220\,\text{MHz}$ batch, systematically $\sim$0.28 % below the nominal value.

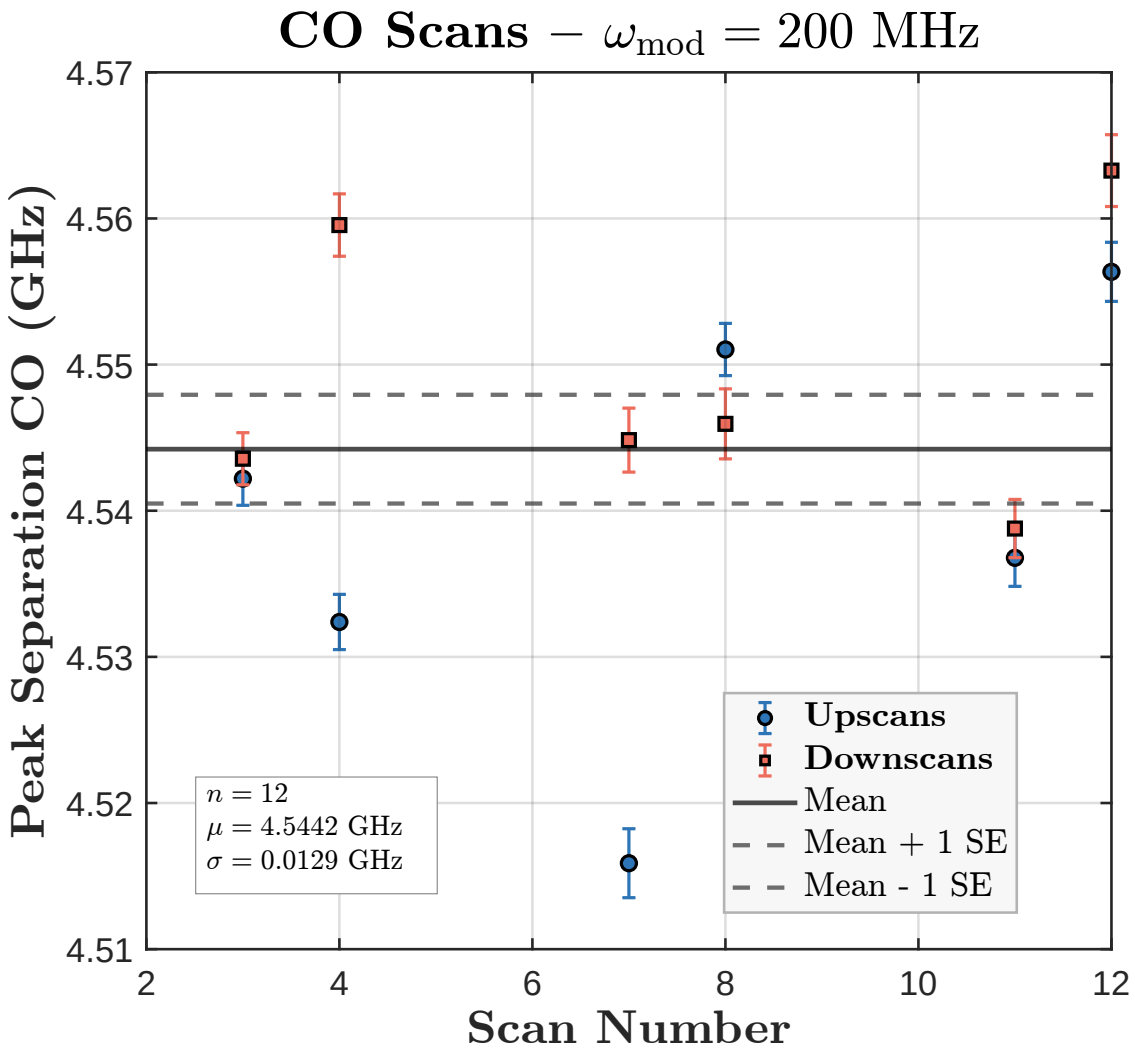


Figure D.4: Scatter of peak separations vs. scan number for co-alignment at $\omega_{\text{mod}} = 200\,\text{MHz}$, in chronological order.

# Appendix E

# Uncertainty propagation and Monte Carlo verification

## E.1 Within-fit correlations and error propagation

The four fit parameters $(m_{co}, b_{co}, m_{ctr}, b_{ctr})$ come from two completely independent datasets, so there are no correlations between the two fits. Within each fit, however, slope and intercept are correlated because they are estimated from the same data, with covariance

$$\mathrm{cov}(m, b) = -\frac{\sum w_i \, x_i}{\sum w_i \sum w_i x_i^2 - \left(\sum w_i x_i\right)^2}, \tag{E.1}$$

where $w_i = 1/\sigma_i^2$ are the scan weights and $x_i$ the modulation frequencies. This covariance is negative when the mean of the $x$-values is positive, which is the case here. Including these within-fit correlations is essential: the slope and intercept errors enter the propagation with opposite-sign cross terms, and the negative covariance produces a large partial cancellation. Ignoring it inflates the final uncertainties by roughly an order of magnitude.

The general error-propagation formula for a function $f(x_1, x_2, \ldots)$ is

$$\sigma^2(f) = \sum_i \left(\frac{\partial f}{\partial x_i}\right)^2 \sigma^2(x_i) + 2 \sum_{i<j} \frac{\partial f}{\partial x_i} \frac{\partial f}{\partial x_j} \, \mathrm{cov}(x_i, x_j). \tag{E.2}$$

Since parameters from different fits are uncorrelated, the only non-zero covariance terms are $\mathrm{cov}(m_{co}, b_{co})$ and $\mathrm{cov}(m_{ctr}, b_{ctr})$. We use the shorthand $N = b_{ctr} - b_{co}$ and $D = m_{co} - m_{ctr}$.

**Uncertainty in $\omega_{\mathrm{mod}}^{\mathrm{int}}$.** Applying Eq. (E.2) to $\omega_{\mathrm{mod}}^{\mathrm{int}} = N/D$, the partial derivatives are

$$\frac{\partial \omega_{\mathrm{mod}}^{\mathrm{int}}}{\partial b_{co}} = -\frac{1}{D}, \qquad \frac{\partial \omega_{\mathrm{mod}}^{\mathrm{int}}}{\partial b_{ctr}} = +\frac{1}{D}, \tag{E.3}$$

$$\frac{\partial \omega_{\mathrm{mod}}^{\mathrm{int}}}{\partial m_{co}} = -\frac{N}{D^2}, \qquad \frac{\partial \omega_{\mathrm{mod}}^{\mathrm{int}}}{\partial m_{ctr}} = +\frac{N}{D^2}. \tag{E.4}$$

Substituting into Eq. (E.2) gives

$$\boxed{\sigma^2(\omega_{\mathrm{mod}}^{\mathrm{int}}) = \frac{1}{D^2}\Bigg[\sigma^2(b_{co}) + \sigma^2(b_{ctr}) + \frac{N^2}{D^2}\big(\sigma^2(m_{co}) + \sigma^2(m_{ctr})\big) + \frac{2N}{D}\big(\mathrm{cov}(m_{co}, b_{co}) + \mathrm{cov}(m_{ctr}, b_{ctr})\big)\Bigg]} \tag{E.5}$$

**Uncertainty in $PS^{\mathrm{int}}$.** Substituting Eq. (6.20) into (6.21) yields

$$\begin{aligned} PS^{\mathrm{int}} &= m_{co} \cdot \frac{b_{ctr} - b_{co}}{m_{co} - m_{ctr}} + b_{co} \\ &= \frac{m_{co}(b_{ctr} - b_{co}) + b_{co}(m_{co} - m_{ctr})}{D} \\ &= \frac{m_{co}\, b_{ctr} - m_{ctr}\, b_{co}}{D}. \end{aligned} \tag{E.6}$$

The partial derivatives are

$$\frac{\partial PS^{\mathrm{int}}}{\partial m_{co}} = -\frac{m_{ctr}\, N}{D^2}, \qquad \frac{\partial PS^{\mathrm{int}}}{\partial b_{co}} = -\frac{m_{ctr}}{D}, \tag{E.7}$$

$$\frac{\partial PS^{\mathrm{int}}}{\partial m_{ctr}} = +\frac{m_{co}\, N}{D^2}, \qquad \frac{\partial PS^{\mathrm{int}}}{\partial b_{ctr}} = +\frac{m_{co}}{D}. \tag{E.8}$$

Substituting into Eq. (E.2) gives

$$\boxed{\sigma^2(PS^{\mathrm{int}}) = \frac{1}{D^2}\Bigg[m_{ctr}^2\left(\frac{N^2}{D^2}\,\sigma^2(m_{co}) + \sigma^2(b_{co})\right) + m_{co}^2\left(\frac{N^2}{D^2}\,\sigma^2(m_{ctr}) + \sigma^2(b_{ctr})\right) + \frac{2N}{D}\Big(m_{ctr}^2\,\mathrm{cov}(m_{co}, b_{co}) + m_{co}^2\,\mathrm{cov}(m_{ctr}, b_{ctr})\Big)\Bigg]} \tag{E.9}$$

## E.2 Monte Carlo verification

To verify the analytic formulas above, we run a Monte Carlo simulation. The four fit parameters are sampled $10^6$ times from multivariate normal distributions that include the within-fit correlations:

$$\begin{pmatrix} b_{co} \\ m_{co} \end{pmatrix} \sim \mathcal{N}\left(\begin{pmatrix} \bar{b}_{co} \\ \bar{m}_{co} \end{pmatrix}, \begin{pmatrix} \sigma^2(b_{co}) & \mathrm{cov}(m_{co}, b_{co}) \\ \mathrm{cov}(m_{co}, b_{co}) & \sigma^2(m_{co}) \end{pmatrix}\right), \tag{E.10}$$

$$\begin{pmatrix} b_{ctr} \\ m_{ctr} \end{pmatrix} \sim \mathcal{N}\left(\begin{pmatrix} \bar{b}_{ctr} \\ \bar{m}_{ctr} \end{pmatrix}, \begin{pmatrix} \sigma^2(b_{ctr}) & \mathrm{cov}(m_{ctr}, b_{ctr}) \\ \mathrm{cov}(m_{ctr}, b_{ctr}) & \sigma^2(m_{ctr}) \end{pmatrix}\right), \tag{E.11}$$

with the two draws independent of each other. For each sample, the intersection point is computed from Eqs. (6.20)–(6.21); the standard deviation of the resulting distribution gives the Monte Carlo uncertainty. Figure E.1 shows the histograms of $\omega_{\text{mod}}^{\text{int}}$ and $PS^{\text{int}}$; the analytic and Monte Carlo values agree to within rounding, confirming the derivation.

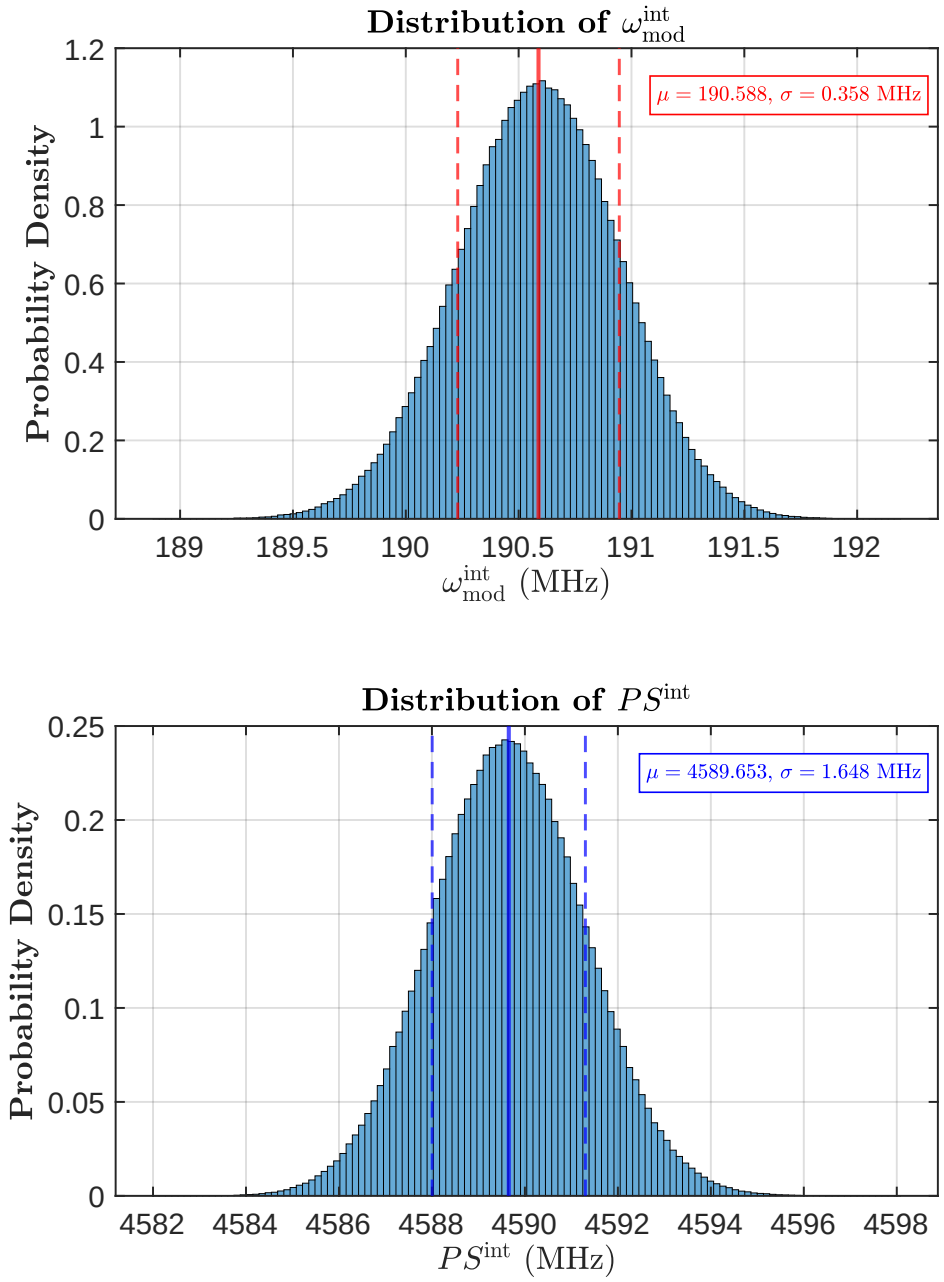


Figure E.1: Monte Carlo distributions of the intersection-point coordinates from $10^6$ samples. Solid lines indicate the mean, dashed lines $\pm 1\sigma$.

# Appendix F

# Lock-in detection

## F.1 Operating principle

Lock-in detection is a phase-sensitive technique that recovers a small signal from a much larger background of broadband noise. A useful analogy is finding your car in a crowded parking lot: among thousands of similar cars, you can't pick yours out by sight. But if you blink your headlights at a known rate, your car instantly stands out, even if it's mostly hidden in the crowd. In our experiment we "blink" the 939 nm pump laser by chopping it with an AOM, which periodically turns the population of intermediate-state atoms on and off. Anything in the 406 nm absorption signal that varies at the chopping frequency must be due to the pump laser; everything else—electrical, acoustic, $1/f$, dark current, ambient light—is rejected by the lock-in.

**Why we still see signal at all.** For the Pb 939 nm transition ($^3P_0 \to {}^3P_2$), the upper state has degeneracy $2J + 1 = 5$, so the thermal population ratio is

$$\frac{N_e}{N_g} = 5\, e^{-\Delta E/k_B T} = 5\, e^{-1.32\,\mathrm{eV}/0.0925\,\mathrm{eV}} \approx 3 \times 10^{-6}, \tag{F.1}$$

with $\Delta E = hc/\lambda \approx 1.32\,\mathrm{eV}$ and $k_B T \approx 0.0925\,\mathrm{eV}$ at $T = 800\,^\circ\mathrm{C}$. Only about three Pb atoms in a million sit in the $^3P_2$ state thermally. But there are roughly $10^{21}$ Pb atoms per gram of sample, so even three-per-million is enough to produce a measurable raw 406 nm absorption from the much stronger $E1$ second-step transition. The pump laser increases the intermediate-state population from $\sim 3$ to $\sim 10$ per million, and this small *laser-induced* change is what the lock-in picks out. Because the thermal excited-state fraction is so small, the ground-state population is essentially unaffected by the pump, and we are far from saturating the first-step transition.

**The lock-in operation.** Let $A_{\mathrm{sig}}(t)$ be the absorption signal at the photodetector that is correlated with the pump-laser chopping, and let $N(t)$ be the broadband noise. The raw

photodetector voltage is

$$V_{\text{raw}}(t) = A_{\text{sig}}(t) + N(t). \tag{F.2}$$

The lock-in amplifier multiplies this raw signal by an internal reference waveform synchronized to the AOM chopping frequency,

$$V_{\text{ref}}(t) = \text{sgn}[\sin(\omega_{\text{chop}} t + \phi)]\,, \tag{F.3}$$

where $\phi$ is the phase between the reference and the actual signal (set to zero in the ideal case). The mixed product $V_{\text{mix}}(t) = V_{\text{raw}}(t) \cdot V_{\text{ref}}(t)$ is then low-pass filtered, equivalent to averaging over a sliding integration window of duration $\tau$,

$$V_{\text{out}}(t) = \frac{1}{\tau} \int_{t-\tau}^{t} V_{\text{raw}}(t')\, V_{\text{ref}}(t')\, dt'. \tag{F.4}$$

The signal component $A_{\text{sig}}(t)$ is in-phase with the reference and therefore adds to the integral, giving a non-zero DC value. The noise $N(t)$ is incoherent with the reference—equally likely to be positive or negative within any given chopping cycle—so its contribution to the integral averages to zero for $\tau$ long enough to cover many chopping periods. Slowly varying or DC backgrounds (room light, dark current, baseline absorption) sit at zero frequency and are also rejected: when multiplied by the reference, the positive and negative half cycles cancel exactly, and the integral over any whole number of chopping periods is zero.

**Simulation.** Figure F.1 illustrates the operation step by step using a simulated noisy signal. Panel 0 shows the small chopped signal alongside the much larger broadband noise; panel 1 shows the sum, in which the signal is invisible to the eye. Panel 2 shows the reference signal. Panel 3 shows the mixed product $V_{\text{raw}} \cdot V_{\text{ref}}$, which still looks noise-dominated. Panel 4 shows the result of the sliding integration over $\tau = 4\,\text{ms}$: a clean DC signal emerges from the noise. As the first-step laser is slowly scanned across the atomic line, this DC signal slowly traces out the underlying line shape.

If the pump laser is left unchopped, the underlying signal is a constant rather than an oscillation at $\omega_{\text{chop}}$. When multiplied by the reference and integrated, the result averages to zero (Fig. F.2, panel 4). This is the sense in which chopping "breaks the symmetry": it puts the signal of interest at the reference frequency where the lock-in is sensitive, while everything else remains at frequencies the lock-in rejects.

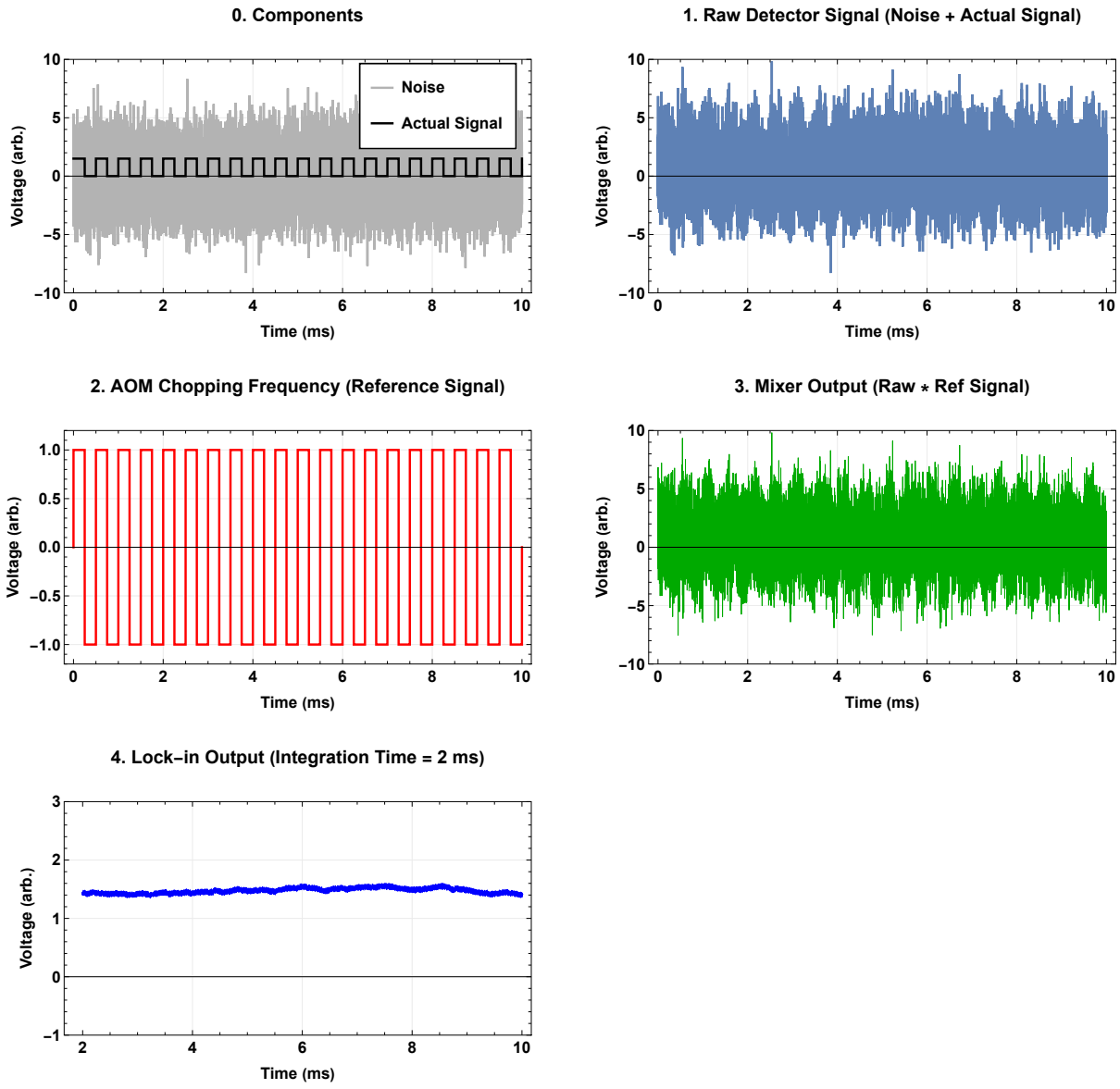


Figure F.1: Lock-in detection with AOM chopping. Panels 0–4: the true signal and the noise; their sum at the photodetector; the reference waveform; the mixer output; and the integrated lock-in output, which recovers a clean DC signal from a noise floor that buries the raw trace.

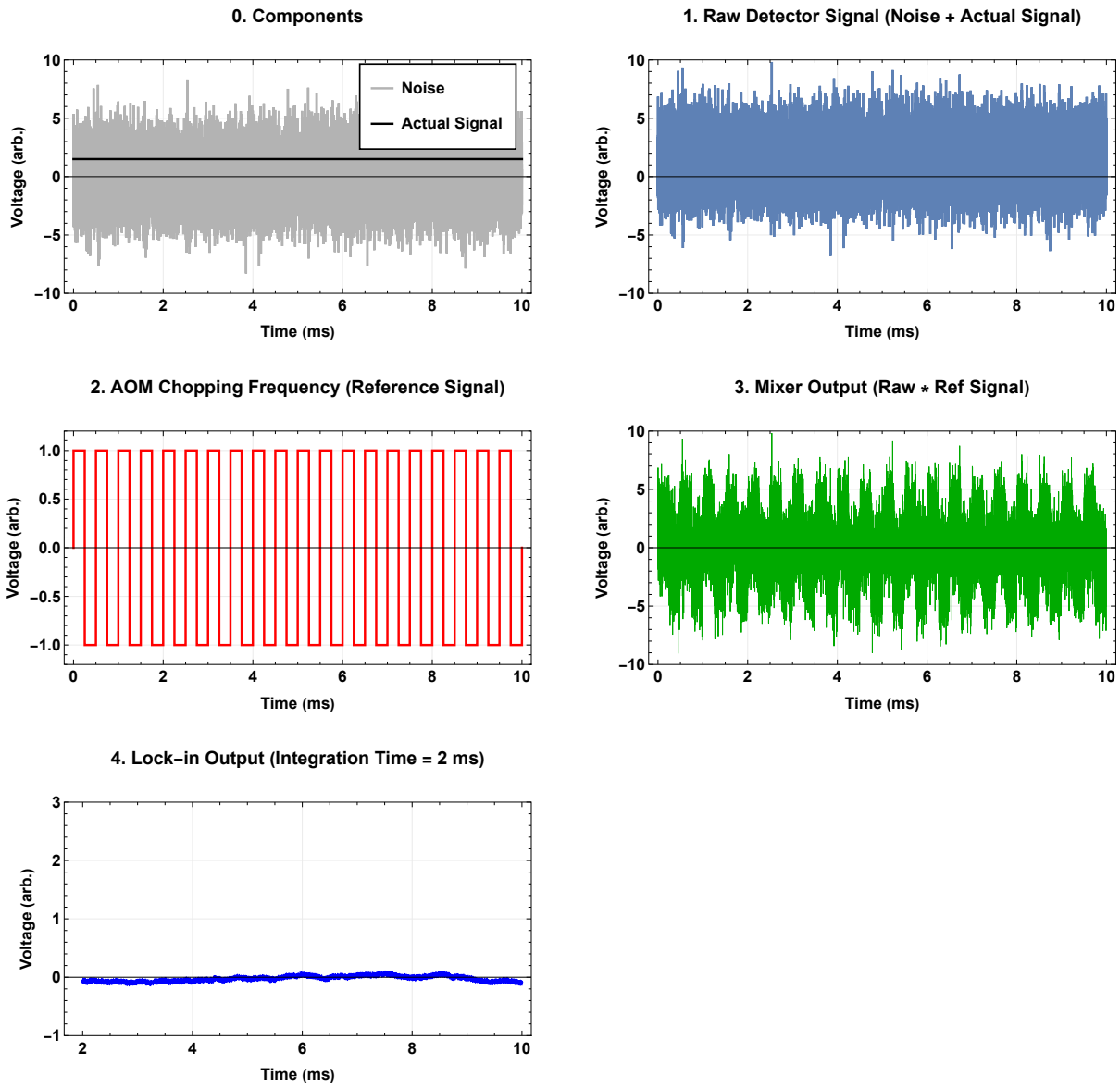


Figure F.2: Lock-in detection without AOM chopping. With no modulation at the reference frequency, the integrated output averages to zero.

# Appendix G

# Pb electronic structure details

## G.1 Electron configuration

Neutral lead has the electron configuration

$$\mathrm{Pb} : [\mathrm{Xe}]\, 4f^{14}5d^{10}6s^2 6p^2,$$

where [Xe] denotes a closed xenon core (54 electrons). In atomic physics, the filled inner shells $4f^{14}5d^{10}6s^2$ are often treated as an inert core, leaving two valence electrons in $6p^2$, which determine the low-energy spectroscopy.

## G.2 Term symbols

Electronic states are labeled by term symbols of the form

$$^{2S+1}L_J,$$

which describe a many-electron eigenstate of the atom. Be careful to distinguish between lower-case and upper-case letters: the former represents orbitals and the latter angular momentum. Here $S$ is the total electron spin, $2S+1$ is the spin multiplicity, $L$ is the total orbital angular momentum (with $S, P, D, F \equiv L = 0, 1, 2, 3$), and $J$ is the total angular momentum from $\mathbf{J} = \mathbf{L} + \mathbf{S}$.

## G.3 The Pb $6p^2$ ground manifold

For the Pb $6p^2$ ground manifold, the relevant states are

$$^3P_J \quad (J = 0, 1, 2),$$

meaning $S = 1$, $L = 1$, and $J = |L - S|, \ldots, L + S = 0, 1, 2$. Due to relativistic effects and spin-orbit coupling, these electronic states are no longer degenerate, leading to fine structure.

# Bibliography


[1] M. S. Safronova, D. Budker, D. DeMille, D. F. J. Kimball, A. Derevianko, and C. W. Clark, Rev. Mod. Phys. **90**, 025008 (2018), URL `https://link.aps.org/doi/10.1103/RevModPhys.90.025008`.

[2] C. Yang, Bachelor's thesis, Williams College (2024).

[3] R. S. Wang, Bachelor's thesis, Williams College (2024).

[4] C. J. Foot, *Atomic Physics*, Oxford Master Series in Physics (Oxford University Press, Oxford, 2005), ISBN 9780198506966.

[5] C. Anderson, Bachelor's thesis, Williams College (2025).

[6] A. C. Kinny, Bachelor's thesis, Williams College (2024).

[7] Thorlabs, Inc., *Lny1010f 10 ghz phase modulator spec sheet*, `https://media.thorlabs.com/globalassets/items/l/ln/lny/lny1010f/ttn313025-s01.pdf` (2026), product specification sheet (accessed 2026-05-01).

[8] R. Paschotta, *Electro-optic modulators*, `https://www.rp-photonics.com/electro_optic_modulators.html` (accessed 2026), rP Photonics Encyclopedia.

[9] O. Svelto, *Principles of Lasers* (Springer, 2010), 5th ed.

[10] S. C. Doret, The Review of scientific instruments **89 2**, 023102 (2017), URL `https://api.semanticscholar.org/CorpusID:3680471`.

[11] M. Born and E. Wolf, *Principles of Optics* (Cambridge University Press, 1999), 7th ed.